ABSTRACT

Title of Document: INSIGHTS TO THE GENETICS, AGE AND CRYSTALLIZATION OF GROUP IC AND IIC IRON METEORITES

Hope Tornabene, Master of Science, 2020

Directed By: Professor Richard J. Walker Department of Geology

Siderophile element isotopic compositions and abundances were determined for the IC and IIC iron meteorite groups to assess whether the members of each group can be related by crystal-liquid fractionation models, constrain timing of metal-silicate segregation and parent body accretion, and characterize the chemical characteristics of the parent bodies.

Collectively, the IC and IIC group meteorites sample two genetically distinct reservoirs that were nevertheless chemically similar with respect to HSE absolute and relative abundances. Further, the relative core sizes of the IC and IIC parent bodies were similar, consistent with similar states of planetesimal oxidation. The distinct chemical trends between within the two groups originated as a result of their unique formation histories, revealing that mixing and impact processes were important mechanisms in the early protoplanetary disk.

Insights to the Genetics, Age, and Crystallization of Group IC and IIC Iron Meteorites

by
Hope A. Tornabene

Thesis submitted to the Faculty of the Graduate School of the
University of Maryland, College Park in partial fulfillment
of the requirements for the degree of
Master of Science
2020

Advisory Committee:

Professor Richard J. Walker, Chair
Research Scientist Richard D. Ash
Associate Professor Ricardo Arevalo, Jr.

Table of Contents

List of Tables

List of Figures

Chapter 1: Introduction and Goals

1.1. Introduction to Iron Meteorites

Meteorites are recovered fragments of small rocky objects in our solar system that have fallen to Earth. Iron meteorites consist largely of metallic iron and nickel. Members of iron meteorite groups are deduced to be chemically related to one another through a common physical process on the same parent body (e.g., Schaudy et al., 1972; Scott and Wasson 1975). Iron meteorite groups are classified into two broad categories based on their believed mechanisms of formation: "magmatic" and "non-magmatic". Magmatic iron meteorite groups are characterized by little variation in Ni and Ge concentrations because crystal-liquid fractionation does not strongly modify their concentrations within crystallizing metallic cores. Members of a group are commonly inferred to have formed by fractional crystallization of cores of melted planetesimals, fueled by the decay of the extinct ^{26}Al. By contrast, non-magmatic iron meteorite groups can exhibit large variations in Ni and Ge that cannot be explained by fractional crystallization. Most non-magmatic meteorites likely formed by rapid solidification of metal segregating from silicates within large melt sheets produced by the heat of impacts.

Classification of iron meteorites is also dependent on volatile siderophile element (e.g., Ga, Ge) depletion within the meteorites. Roman numerals I-IV are used in the classification, where I is the least depleted and IV is the most depleted in volatile siderophile elements. Magmatic and non-magmatic iron meteorites can also be classified based on their mineralogic structure (presence/nature of Widmanstätten pattern).

Based on limited ranges in Ni and Ge concentrations, group IC and IIC iron meteorites have been classified as magmatic irons (Scott, 1977; Wasson, 1969). Thirteen meteorites

are currently classified as belonging to the IC group. The IC group is characterized by a range of diverse mineral structures, including coarse octahedrites, medium octahedrites, and polycrystalline irons. Octahedrite refers to the structural class of iron meteorites and is indicative of the dimensions of kamacite and taenite lamellae For example, coarse octahedrites contain lamellae widths that are greater than ~3mm. Eight meteorites are currently classified as belonging to the IIC group. Group IIC irons are structurally classified as plessitic octahedrites (fine-grained lamellae), with chemical compositions characterized by minor depletions in the more volatile siderophile elements, such as Ga and Ge.

The highly siderophile elements (HSE) are useful in determining the crystallization histories of the magmatic iron meteorite groups, due to their predictable behavior during magmatic processes (Pernicka and Wasson, 1987; Chabot and Jones, 2003; McCoy et al., 2011). This study uses high precision HSE data for bulk samples to examine the the relationships of meteorites within the IC and IIC groups, as well as provide insight into the composition and evolution of their parental metallic cores.

1.2. Iron Meteorite Genetics

In addition to the classification scheme based on chemical composition and texture, iron meteorites (and other meteorites) currently are divided into two genetic "types". Nucleosynthetic "genetic" isotope anomalies in bulk planetary materials are characterized by mass independent variations in certain isotope ratios that can differ from the bulk silicate Earth. The variations are consistent with nucleosynthetic theory and direct isotopic measurements of presolar grains found in primitive meteorites (Arlandini et al., 1999;

Burkhardt et al., 2011). The nucleosynthetic anomalies present in bulk planetary materials likely developed by heterogeneous accretion of presolar components to the parent bodies. This could result from condensation or evaporation effects, location within the nebula, timing, or any combination of these (Trinquier et al., 2007; Warren, 2011; Kruijer et al., 2017).

Variations in genetic isotopic characteristics have been used to subdivide meteorites into carbonaceous chondrite (CC) and non-carbonaceous (NC) types (Warren, 2011). Molybdenum and Ru are particularly useful for tracing isotopic heterogeneity in iron meteorites because both elements are siderophile and have seven stable isotopes synthesized by the *p*-process (^{92}Mo, ^{94}Mo, ^{96}Ru, ^{98}Ru), *s*-process (^{96}Mo, ^{100}Ru), *r*-process (^{100}Mo, ^{104}Ru), and both the *s*- and *r*- processes (^{95}Mo, ^{97}Mo, ^{98}Mo ^{99}Ru, ^{101}Ru, ^{102}Ru).

The CC type is distinguished from the NC type by having an excess of *r*-process (and possible *p*-process) component isotopes (Burkhardt et al., 2011). Based on Mo isotopic compositions, Kruijer et al., (2017) and Poole et al., (2017) concluded that the IIC group is of the CC type and the IC group is of the NC type. It has been postulated that CC and NC group meteorites formed in discrete feeding zones outboard and inboard of the proto-Jupiter, respectively, and possibly at different times (Krujier et al., 2017). Therefore, comparing and contrasting the IC irons with the IIC irons allows for assessment of the different nebular domains, a major goal of this study.

1.3. Hf-W Chronology

The ^{182}Hf-^{182}W system ($t_{1/2}$ = 9 Ma; Vockenhuber et al., 2004) can be used to assess the thermal evolution of parent bodies with respect to the timing of metal-silicate segregation.

It is assumed that metal was instantaneously segregated from a metal-silicate mixture on a parent body with a chondritic Hf/W ratio (Kruijer et al. 2017; Hilton et al. 2019). The ^{182}W value recorded in iron meteorites reflects the isotopic composition at the time Hf (lithophile) separated from W (siderophile). A model age of metal segregation (ΔT_{CAI}) in iron meteorites can be calculated relative to the initial $\mu^{182}W$ value determined for calcium-aluminum-rich inclusions (CAI) of -349 ± 7 (Kruijer et al., 2014b), and assuming a present day chondritic $\mu^{182}W$ value of -191 ± 8 (Kleine et al., 2004) using the equation:

$$\text{Eq. 1.1: } \Delta T_{CAI} = -\frac{1}{\lambda} \ln \left[\frac{(\mu^{182}W)_{Sample} - (\mu^{182}W)_{Chondrite}}{(\mu^{182}W)_{CAI} - (\mu^{182}W)_{Chondrite}} \right]$$

where λ is the ^{182}Hf decay constant (0.078 ± 0.002; Vockenhuber et al., 2004). The μ notation corresponds to the deviation, in parts per million, of an isotopic ratio of a sample relative to the ratio measured in a laboratory standard. Calcium-aluminum-rich inclusions are the oldest dated solids and their $\mu^{182}W$ value is used to define the age of the solar system.

The NC groups have model ages ~0.3 to 1.0 Ma after CAI formation while the CC groups have relatively younger model ages ~1.1 to 1.4 Ma after CAI formation (Kruijer et al., 2017; Hilton et al., 2019), albeit with uncertainties, these ages partially overlap. The Hf-W system, therefore, allows for the exploration of the timescales and processes of planetary accretion and differentiation.

Chapter 2: Genetics, Age and Crystallization History of Group IIC Iron Meteorites

Note: This chapter is currently in press in *Geochimica et Cosmochimica Acta*. For this chapter, siderophile element abundances were collected by laser ablation ICP-MS with the help of Richard Ash. Rich Walker helped in the collection of highly siderophile element and Re-Os data. I conducted the chemistry and collected Os, Mo, Ru and W isotope analysis with help from Katherine Bermingham and Connor Hilton. Connor Hilton provided results for thermal modelling from the data I collected. I interpreted the data, with the help of Connor Hilton and Rich Walker, and wrote the first draft to the manuscript, and co-authors provided edits.

Abstract

The eight iron meteorites currently classified as belonging to the IIC group were characterized with respect to the compositions of 21 siderophile elements. Several of these meteorites were also characterized for the isotopic compositions of Mo, Ru and W, to characterize their nucleosynthetic signatures, and core differentiation ages. Chemical and isotopic data for one, Wiley, indicate that it is not a IIC iron meteorite and should be reclassified as ungrouped. The remaining seven IIC iron meteorites exhibit broadly similar bulk chemical and isotopic characteristics, consistent with an origin from a common parent body. Variations in highly siderophile element (HSE) abundances among the members of the group can be well accounted for by a fractional crystallization model with all the meteorites crystallizing between ~10 and ~26% of the original melt, assuming initial S and P concentrations of 8 wt.% and 2 wt.%, respectively. Abundances of HSE estimated for the parental melt suggest a composition with chondritic relative abundances of HSE ~6 times higher than in bulk carbonaceous chondrites, consistent with the IIC irons sampling a parent body core comprising ~17% of the mass of the body.

Radiogenic ^{182}W abundances of two group IIC irons, corrected for a nucleosynthetic component, indicate a metal-silicate segregation age of 3.2 ± 0.5 Myr subsequent to the formation of Calcium-Aluminum-rich Inclusions (CAI). When this age is coupled with thermal modeling, and assumptions about the Hf/W of precursor materials, a parent body accretion age of 1.4 ± 0.5 Myr (post-CAI) is obtained.

The IIC irons and Wiley have ^{100}Ru mass independent "genetic" isotopic compositions that are identical to other irons with so-called carbonaceous chondrite (CC) type genetic affinities, but enrichments in ^{94,95,97}Mo and ^{183}W that indicate greater *s*-process deficits relative to most known CC iron meteorites. If the IIC irons and Wiley are of the CC type, this indicates variable *s*-process deficits within the CC reservoir, similar to the *s*-process variability within the NC reservoir observed for iron meteorites. Nucleosynthetic models indicate that Mo and ^{183}W *s*-process variability should correlate with Ru isotopic variability, which is not observed. This may indicate the IIC irons and Wiley experienced selective thermal processing of nucleosynthetic carriers, or are genetically distinct from the CC and NC precursor materials.

2.1. Introduction

Members of magmatic iron meteorite groups are presumed to sample planetesimal cores, with members of each group chemically related through common physical processes, such as fractional crystallization and solid-liquid metal mixing (e.g., Schaudy et al., 1972; Scott and Wasson, 1975; Pernicka and Wasson, 1987). Group IIC meteorites comprise a magmatic iron group with chemical compositions characterized by minor depletions in some volatile siderophile elements, such as Ga and Ge. They are structurally classified as

plessitic octahedrites. Based on similar Ni, Ir and Ge concentrations, eight meteorites are currently classified as group IIC magmatic irons (Wasson, 1969; *Meteoritical Bulletin,* 2020).

In addition to chemical similarities, members of a magmatic group should also be characterized by the same nucleosynthetic isotope compositions, given that they are presumed to have crystallized from the same melt. Nucleosynthetic, or "genetic," isotope anomalies in bulk planetary materials are defined by mass independent variations in certain isotope ratios that differ from those determined for the bulk silicate Earth. The variations are consistent with nucleosynthetic theory and direct isotopic measurements of presolar grains found in primitive meteorites (Arlandini et al., 1999; Burkhardt et al., 2011). The nucleosynthetic anomalies present in bulk planetary materials likely developed by heterogeneous accretion of presolar components to parent bodies. This could result from condensation or evaporation effects, location within the nebula, timing, or any combination of these (e.g., Trinquier et al., 2007; Trinquier et al., 2009; Warren, 2011).

Variations in genetic isotopic characteristics have been used to subdivide meteorites into "carbonaceous chondrite" (CC) and "non-carbonaceous" (NC) types (Warren, 2011). It has been postulated that CC and NC type meteorites formed in discrete feeding zones outboard and inboard of the proto-Jupiter, respectively, and possibly at different times (Warren, 2011; Kruijer et al., 2017; Nanne et al., 2019). For iron meteorites, the excess of *r*-, and potentially *p*-process isotopes of the siderophile element Mo are especially useful for distinguishing CC from NC parent bodies (e.g., Budde et al., 2016; Poole et al., 2017; Worsham et al., 2017, 2019). Based on Mo isotopes, Kruijer et al. (2017) and Poole et al. (2017) concluded that the IIC group is of the CC type.

The ^{182}Hf-^{182}W system ($t_{1/2}$ = 9 Myr; Vockenhuber et al., 2004) can be used to assess the thermal evolution of magmatic iron meteorite parent bodies with respect to both the timing of metal-silicate segregation (i.e., core formation), and the accretion age of the parent body. Model accretion ages are obtained by combining the model segregation ages with thermal models and assumptions about the size, ^{26}Al content, and Hf/W of precursor materials and the parent body (e.g. Kruijer et al. 2017; Hilton et al. 2019). The NC type groups have model accretion ages ranging from 0.3 ± 0.3 to 1.0 ± 0.5 Myr after calcium aluminum rich inclusion (CAI) formation while the CC type groups, on average, have relatively younger model accretion ages of 1.1 ± 0.6 to 1.4 ± 0.5 Myr after CAI formation (Kruijer et al., 2017; Hilton et al., 2019). It has recently been suggested, however, that Hf/W in at least some NC bodies may have been less than in CC parent bodies (Hellmann et al., 2019). If so, this could mean that model accretion ages for some NC bodies are more similar to, or even younger than model accretion ages for CC bodies.

The objectives of this study are to further investigate the chemical and genetic characteristics of the IIC group, assess if any/all meteorites comprising the group can be related by a crystal-liquid fractionation model, further constrain timing of metal-silicate segregation and parent body accretion, and model the chemical characteristics of the parent body.

2.2. Samples

Five meteorite samples were obtained from the Smithsonian Institution National Museum of Natural History: Ballinoo (USNM 3284), Kumerina (USNM 5711), Perryville (USNM 428), Salt River (USNM 1131) and Wiley (USNM 1328). Cratheús (1950) and the

IVA iron meteorite Pará de Minas were obtained from the Museu Nacional/UFRJ, Brazil. Unter Mässing (MPK 3074A) was obtained from Senckenberg Forschungsinstitut und Naturmuseum, Germany. Darinskoe was obtained from the Geological Museum of the Geological and Geophysical Institute of the Siberian Branch, Russia. A meteorite identified as Cratheús (1950) (ME 2712) was obtained from the Field Museum (Chicago).

2.3. Analytical Methods

2.3.1. Laser Ablation ICP-MS

The ten samples were cut into 0.03-0.13 g pieces using a diamond blade saw with high purity water as a coolant and lubricant. The cut samples were polished with carborundum paper until one flat surface was free of diamond blade markings. To remove any contamination from the blade and carborundum paper, each sample was ultrasonicated in ethanol for approximately one minute after preparation. Siderophile element concentrations were obtained for polished surfaces by laser ablation using a *New Wave* UP213 ultraviolet laser coupled to a *Thermo-Finnigan Element 2* inductively coupled plasma mass spectrometer (ICP-MS). Laser ablation was achieved with a repetition rate of 7 Hz and laser output was varied to maintain an energy flux of ~2-4 Jcm^{-2}. All data were processed using *LAMTRACE* (Rusk, 2009) using known concentrations of reference materials (iron meteorites Hoba and Filomena). Initially, Fe was used as an internal standard for the IIC group using accepted values in the literature (Buchwald, 1975; Wasson, 1969), then all concentrations were recalculated to force Fe, Ni, and Co concentrations to sum to 100%.

2.3.2. ^{187}Re-^{187}Os and siderophile element analysis

Bulk sample isotope dilution measurements of the highly siderophile elements (HSE) Re, Os, Ir, Ru, Pt and Pd were performed on ~50-100 mg pieces of polished chips using combined multi-collector ICP-MS and thermal ionization mass spectrometry (TIMS). The chemical-separation techniques used have been previously described (e.g., Walker et al., 2008). In brief, appropriate amounts of separate ^{185}Re-^{190}Os and ^{191}Ir-^{99}Ru-^{194}Pt-^{105}Pd mixed spikes were added to each sample. Each mixture (sample and spike) was sealed and digested in *Pyrex*™ Carius tubes along with 5 mL of high purity concentrated HNO_3 and 2.5 mL of high purity concentrated HCl. The tubes were then heated to approximately 230˚C for ≥24 hours. After heating, Os was separated using a carbon tetrachloride solvent extraction method (Cohen and Waters, 1996) and further purified by microdistillation (Birck et al., 1997). The Os total processing blank was 2 ± 1 pg (n = 3), which was negligible relative to the quantities of Os extracted from the samples. Approximately 80-200 ng of purified Os were loaded onto an outgassed Pt filament along with Ba hydroxide activator and analyzed as OsO_3^- by a *Thermo Fisher Triton* TIMS using standard techniques. Osmium isotope dilution data were corrected for natural and instrumental mass fractionation by normalizing $^{190}Os/^{188}Os$ to 3.08271 (Allègre and Luck, 1980).

Rhenium and the remaining HSE were dissolved in low molarity hydrochloric acid, and extracted and separated using anion exchange columns (Rehkämper and Halliday, 1997). Each sample was loaded into a column with 1 M HCl, then Re and Ru were eluted with 12 mL 6 M HNO_3, Ir and Pt were eluted with 12 mL concentrated HNO_3, and Pd was eluted with 15 mL concentrated HCl. The aliquots of Re and Ru were then dried and re-dissolved in 1 M HCl and loaded onto a smaller anion column for further purification. The

Re, Ir, Ru, Pt and Pd blanks for this procedure averaged 4 ± 2, 5 ± 7, 40 ± 10, 40 ± 4 and 100 ± 100 pg, respectively (n = 3). All analyses were blank corrected but the corrections had negligible impact on analytical uncertainties. Rhenium, Ru, Ir, Pt and Pd were analyzed using a *Thermo Neptune Plus* multi-collector ICP-MS. Tungsten was added to Re solutions to correct for mass fractionation. Estimated uncertainties for Re and Os are ~0.1%. Uncertainties for other HSE are better than 1%.

High precision measurements of Os, Mo, Ru and W isotopic compositions were achieved by dissolving approximately 2-4 g pieces of the meteorites in ~50 mL 8 M HCl at 130 °C for at least 48 hours in Teflon® beakers. The resulting solution was centrifuged and the supernatant was separated into four aliquots to be separately processed for Os, Mo, Ru and W isotopic measurements. Osmium isotopic analysis for cosmic ray exposure (CRE) effects were accomplished by the same chemical separation and purification techniques as discussed above for Os analysis by isotope dilution. Approximately 100-300 ng Os were loaded onto outgassed Pt filaments, covered with Ba hydroxide, and analyzed as OsO_3^- using a *Thermo Fisher Triton* TIMS and standard techniques (e.g., Walker, 2012). Osmium isotopic data were corrected for natural and instrumental mass fractionation by normalizing $^{190}Os/^{188}Os$ to 3.08271 (Allègre and Luck, 1980).

All isotopic compositions in this study are reported using the μ notation, which corresponds to the deviation in parts per million of an isotopic ratio of a sample relative to the ratio measured in a laboratory standard (e.g., Os):

$$\text{Eq. 2.1: } \mu^{189}\text{Os} \left(\frac{\frac{189}{188}\text{Os}_{\text{sample}}}{\frac{189}{188}\text{Os}_{\text{standard}}} - 1 \right) * 10^6$$

During the course of measurements for this study, the external (2σ) reproducibility of repeated analyses of the laboratory Os standard was ± 8 ppm for $\mu^{189}Os$ (*n*=9).

The chemical separation and purification techniques for Mo have been described in Worsham et al. (2016). Aliquots of Mo were dissolved in 1 M HF, loaded onto an anion column with ~1.4 mL AG 1 x 8 200-400 mesh resin, and eluted with 6 M HNO_3 – 3 M HF. Then, the samples were dried, dissolved in 6 M HCl, loaded onto a smaller anion column with ~0.3 mL AG 1x8 200-400 mesh resin and eluted with 1 M HCl. This smaller anion column elution was repeated twice. The Mo aliquots were dried, re-dissolved in 6 M HCl and approximately 500-1000 ng Mo were loaded onto outgassed Re filaments along with ~2 µL of 5 µg/µL $La(NO_3)_3$ activator solution. The Mo blank for this procedure was <1 ng. A double filament assembly was used with the same amount of $La(NO_3)_3$ activator on the second filament. Molybdenum was analyzed as MoO_3^- by a *Thermo Fisher Triton Plus* TIMS using data acquisition and reduction methods detailed in Worsham et al. (2016). To correct for O interferences, the $^{100}Mo^{18}O^{16}O_2^-$ species was measured using a 10^{13} Ω resistor-equipped amplifier. Molybdenum isotopic data were corrected for natural and instrumental mass fractionation by normalizing $^{98}Mo/^{96}Mo$ to 1.453171 (Lu and Masuda, 1994). The external (2σ) reproducibility of repeated analyses of the laboratory standard analyzed were ± 17 ppm, ± 15 ppm, and ± 8 ppm for $\mu^{94}Mo$, $\mu^{95}Mo$, and $\mu^{97}Mo$, respectively (*n*=8).

The chemical separation and purification techniques for Ru have been described in Bermingham et al. (2016). Ruthenium aliquots were dissolved in 0.15 M HCl, loaded onto a primary cation column with ~10 mL AG50WX8 200-400 mesh resin and eluted with 0.15 M HCl. The aliquots were then dried, dissolved in 1 M HCl, and loaded onto a secondary anion column with ~3.8 mL AG 1 x 8 200-400 mesh resin and eluted with 8 M HNO_3 and

concentrated HNO_3. Ruthenium was then further purified by microdistillation. The Ru blank for this procedure was <10 pg. Approximately 800-1000 ng Ru were loaded onto outgassed Pt filaments along with barium hydroxide activator and analyzed as RuO_3^- by a *Thermo Fisher Triton Plus* TIMS using data acquisition and reduction methods detailed in Bermingham et al. (2016). The Ru isotopic data were corrected for natural and instrumental mass fractionation by normalizing $^{99}Ru/^{101}Ru$ to 0.745075 (Chen et al., 2010). The external (2σ) reproducibility of repeated analyses of the laboratory standard analyzed was ± 7 ppm for $\mu^{100}Ru$ (n=7).

After drying the 8 M HCl W aliquot, it was re-dissolved in 0.5 M HCl – 0.5 M HF, eluted through an anion column packed with AG 1x8 100-200 mesh resin with 6 M HCl – 1 M HF. This step was repeated three times, each time using progressively less resin and acid (Touboul and Walker, 2012). The W blank for this procedure was <1 ng. The purified W aliquots were dried, dissolved in 1 M HCl – 0.01 M HF and approximately 500-1000 ng W were loaded onto an outgassed single Re filament with 1 µL of 5 µg/µL La-5 µg/µL Gd activator solution and analyzed as WO_3^- by a *Thermo Fisher Triton* TIMS using data acquisition and reduction methods detailed in Archer et al. (2017). Mass interferences from ReO_3^- were monitored and corrected for. Tungsten isotopic data were corrected for natural and instrumental mass fractionation by normalizing $^{186}W/^{184}W$ to 0.92767 (Völkening et al., 1991). The external (2σ) reproducibility of repeated analyses of the laboratory standard analyzed were ± 5 ppm and ± 6 ppm for $\mu^{182}W$ and $\mu^{183}W$, respectively (*n*=7).

2.3.3. Cosmic ray exposure corrections

Cosmic ray exposure (CRE) can modify the isotopic composition of Mo, Ru, and W of iron meteorites (Fischer-Gödde et al., 2015; Worsham et al., 2017; Bermingham et al., 2018). The magnitude of the cosmogenic effects depends on the location of the sample within the meteoroid and the duration of CRE (Fischer-Gödde et al., 2015). Osmium nuclides dominated by *s*- and *r*-process (e.g., ^{189}Os and ^{190}Os) were homogeneously distributed and mixed in the solar protoplanetary disk (Walker, 2012). Consequently, Os isotopes do not show nucleosynthetic variations among iron meteorites. Osmium-189 is used as a sensitive monitor for neutron fluence in iron meteorites due to the predictable way Os isotopes are affected by CRE and because of its comparatively large neutron cross section and thermal resonance integral (Walker, 2012). Based on the analytical uncertainty for the measured ^{189}Os/^{188}Os, it is assumed that the sampled portions of the meteorites with μ^{189}Os values within ± 8 ppm of 0 were minimally affected by CRE.

2.4. Results

2.4.1. Composition analysis by laser ablation ICP-MS

The IIC irons are plessitic octahedrites with kamacite spindle widths of only ~60-70 μm. Therefore, averaging accumulated data obtained from multiple ~5 mm long laser ablation tracks are generally interpreted to be representative of the composition of the interrogated polished surface. Average elemental concentrations obtained by LA-ICP-MS and 2σ variations for multiple lines of analysis for each meteorite are given in Table 2.1. During laser ablation analysis, however, it was noted that phosphide veins were visible in all samples. Siderophile elements are generally in very low abundances in phosphides

compared to average metal, so the siderophile element concentrations averaged along an ablation track that intersected a phosphide vein tended to be lower than tracks that did not intersect a phosphide vein. The siderophile element data obtained for the phosphide veins were not subtracted from the averages. This accounts for some of the absolute abundance heterogeneity observed when comparing data for multiple lines, rather than reflecting heterogeneities in the metal. The concentrations of Ir, Ga, and Ge determined by laser ablation are within 30%, and Ni concentrations are within 10% of the concentrations reported by Wasson (1969).

Bulk composition data, normalized to CI chondrites, are characterized by broadly similar patterns for most IIC irons (Fig. 2.1). Consistent with their group II classification, there is a slight depletion in volatile siderophile elements, such as Ga and Ge, relative to the more refractory siderophile elements, such as W and Re. Patterns are also characterized by major depletions in the multivalent elements V, Cr, P and Zn.

Of note, the siderophile element abundance pattern for Wiley is quite different from that of the other IIC irons. Also, the data we acquired for the Cratheús (1950) sample obtained from the Field Museum did not match the literature values for Cratheús (1950) as reported by Buchwald (1975) and Wasson (1969), or our data for the Cratheús (1950) sample obtained from Museu Nacional, Brazil. Instead, it has a composition that matches literature data for Cratheús (1931), a group IVA iron meteorite (Buchwald, 1975). Of further note, the Cratheús (1950) specimen from the Field Museum and the Pará de Minas specimen from the Museu Nacional, Brazil have siderophile element abundances that are nearly identical for most siderophile elements (Fig. 2.1). Pará de Minas is a group IVA iron.

Table 2.1 Average elemental concentrations obtained by LA-ICP-MS. Group IIC irons are listed from left to right in order of decreasing Re concentration.

	Darinskoe	Perryville	Cratheús (1950)	Kumerina	Ballinoo
Re	1.4 ± 1.0	1.1 ± 0.3	1.0 ± 0.2	0.9 ± 0.2	0.8 ± 0.2
Os	17.4 ± 7.2	15.3 ± 2.9	12.2 ± 1.4	10.8 ± 2.3	10.9 ± 1.9
W	2.8 ± 1.3	1.7 ± 1.5	1.9 ± 0.3	1.7 ± 1.5	1.7 ± 1.2
Ir	13.7 ± 4.6	13.7 ± 3.0	10.7 ± 1.3	9.9 ± 1.7	9.6 ± 1.0
Mo	10.3 ± 4.0	9.0 ± 4.4	8.5 ± 4.8	9.3 ± 2.4	8.9 ± 4.3
Ru	15.9 ± 8.3	15.7 ± 5.7	12.5 ± 1.7	13.6 ± 1.3	11.8 ± 2.4
V	0.6 ± 0.3	b.d.	0.4 ± 0.9	0.03 ± 0.01	0.02 ± 0.02
Pt	17.8 ± 5.8	19.5 ± 3.7	15.0 ± 2.4	15.7 ± 2.2	14.8 ± 1.4
Rh	2.1 ± 0.8	2.0 ± 0.7	1.7 ± 0.2	1.8 ± 0.2	1.7 ± 0.2
Ni	9.7 ± 3.0	10.4 ± 3.1	9.4 ± 2.3	10.5 ± 2.4	9.5 ± 1.9
Co	0.6 ± 0.1	0.6 ± 0.1	0.57 ± 0.02	0.58 ± 0.02	0.57 ± 0.05
Fe[a]	89.0	93.7	91.0	90.3	90.4
Pd	3.8 ± 1.4	3.9 ± 1.4	3.0 ± 0.4	3.9 ± 0.9	3.5 ± 0.9
Cr	103 ± 56	143 ± 96	111 ± 145	101 ± 35	78 ± 51
P	0.3 ± 0.4	1.0 ± 1.2	0.5 ± 0.8	2.4 ± 4.5	1.2 ± 2.1
Mn	b.d.	b.d.	12.1 ± 22.2	b.d.	b.d.
As	7.7 ± 2.5	6.7 ± 2.3	6.2 ± 1.0	5.8 ± 0.3	7.1 ± 2.3
Au	0.8 ± 0.2	1.0 ± 0.1	0.6 ± 0.1	b.d.	0.8 ± 0.0
Ga	49 ± 10	44 ± 12	40 ± 5	42 ± 4	41 ± 5
Ge	112 ± 36	113 ± 42	96 ± 11	108 ± 11	101 ± 13
Zn	0.5 ± 1.6	0.04 ± 0.10	0.2 ± 0.4	0.1 ± 0.2	0.2 ± 0.3
n	*5*	*6*	*8*	*6*	*7*

	Salt River	Unter Mässing	Wiley	Cratheús (Field Museum)	Parà de Minas
Re	0.7 ± 0.1	0.4 ± 0.1	0.2 ± 0.1	0.22 ± 0.03	0.21 ± 0.09
Os	8.2 ± 1.3	4.5 ± 1.3	1.0 ± 0.2	2.8 ± 0.8	2.5 ± 0.3
W	1.5 ± 1.1	2.0 ± 0.9	0.7 ± 0.5	0.3 ± 0.1	0.8 ± 0.9
Ir	8.4 ± 0.6	5.2 ± 1.3	6.8 ± 1.0	2.3 ± 0.4	2.2 ± 0.4
Mo	8.0 ± 2.7	10.1 ± 9.6	13.6 ± 6.2	5.4 ± 0.4	9.0 ± 17.0
Ru	11.3 ± 0.9	10.2 ± 2.3	28.9 ± 10.8	4.9 ± 0.4	4.0 ± 0.4
V	b.d.	b.d.	b.d.	0.028 ± 0.001	0.2 ± 0.7
Pt	16.7 ± 1.9	14.2 ± 5.4	38.9 ± 6.0	6.0 ± 0.8	5.9 ± 0.5
Rh	1.7 ± 0.1	1.7 ± 0.5	4.0 ± 1.1	0.9 ± 0.3	0.8 ± 0.1
Ni	9.3 ± 0.4	10.2 ± 3.9	10.8 ± 2.5	7.4 ± 0.3	6.8 ± 1.2
Co	0.59 ± 0.04	0.57 ± 0.03	0.8 ± 0.1	0.42 ± 0.01	0.41 ± 0.02
Fe[a]	90.0	90.2	88.5	91.0	91.5
Pd	3.5 ± 0.6	3.7 ± 1.1	4.8 ± 1.9	3.9 ± 0.5	3.0 ± 0.9
Cr	66 ± 33	100 ± 47	b.d.	155 ± 5	34 ± 59
P	1.4 ± 2.2	1.5 ± 3.2	0.6 ± 1.0	0.19 ± 0.02	0.06 ± 0.03
Mn	b.d.	b.d.	b.d.	b.d.	1.0 ± 1.1
As	7.9 ± 2.9	10.2 ± 2.7	13.9 ± 3.4	3.6 ± 0.5	4.9 ± 2.6
Au	1.4 ± 0.2	1.3 ± 1.0	1.1 ± 0.1	b.d.	0.9 ± 0.1
Ga	41 ± 4	40 ± 6	45 ± 2	2.2 ± 0.3	3.7 ± 3.2
Ge	109 ± 13	103 ± 9	129 ± 10	b.d.	b.d.
Zn	0.1 ± 0.1	0.1 ± 0.1	0.02 ± 0.01	0.008 ± 0.004	0.1 ± 0.2
n	*6*	*13*	*6*	*6*	*4*

Nickel, Co, Fe and P concentrations reported in wt.%, all others reported in ppm.

The 2σ values reported were determined from the reproducibility of the number of lines measured (*n*) for each sample.

b.d. Concentration data below detection limits.

[a] Fe data were used as an internal standard.

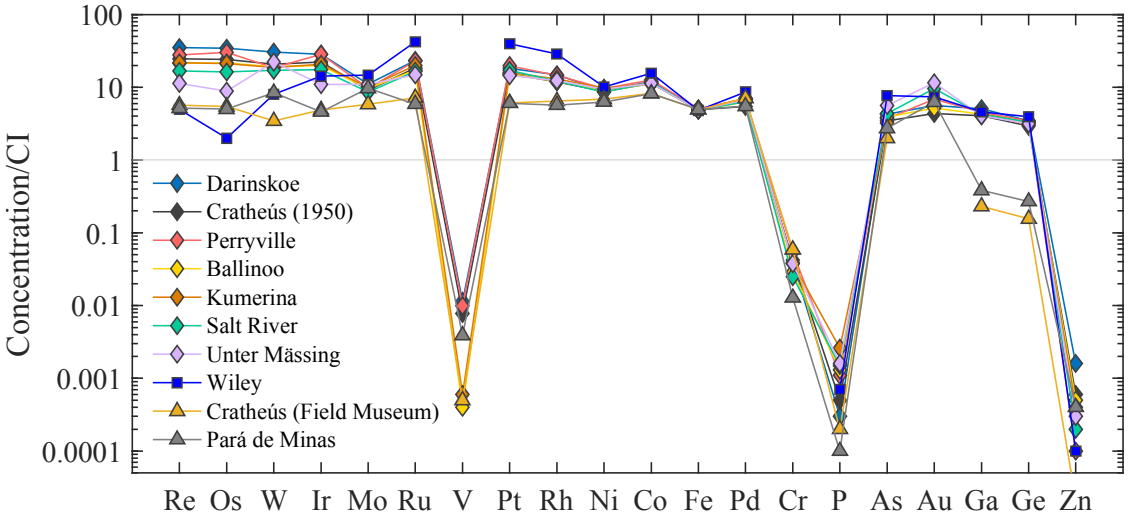

Figure 2.1 CI chondrite normalized abundances of siderophile elements for the IIC irons, Wiley and Pará de Minas. Elements are listed in order of decreasing 50% condensation temperatures from left to right. Bulk composition data were normalized to data for CI chondrites (Lodders and Fegley, 1998).

2.4.2. Highly siderophile element concentrations

The HSE concentration data for bulk samples obtained by isotope dilution are presented in Table 2.2. The concentrations of Re, Ru and Pd obtained by isotope dilutions are all within 30%, and Os, Ir and Pt concentrations are all within 20% of the concentrations obtained by LA-ICP-MS. Chondrite normalized data for most of the meteorites form nested patterns that do not cross with the patterns of other IIC irons. The HSE abundance patterns for the IIC irons, proceeding from lower to higher Ni, and excluding Wiley, are characterized by decreasing abundances of Re, Os, Ir, Ru, and Pt, with little change in Pd (Fig. 2.2). Consistent with the LA-ICP-MS data, the isotope dilution HSE patterns for Cratheús (1931) from the Field Museum and Pará de Minas are essentially identical (Table 2.2; Fig. 2.2). Thus, we conclude that the Field Museum Cratheús (1931) is likely mislabeled as Cratheús (1950). We also infer that Cratheús (1931) and Pará de Minas are the same meteorite.

Table 2.2 Osmium isotopic and HSE composition data, obtained by isotope dilution, for IIC irons, Wiley, Cratheús (1931) and Pará de Minas.

Sample	Wt.	Re	Os	Ir	Ru	Pt	Pd	$^{187}Os/^{188}Os$	2σ	$^{187}Re/^{188}Os$	2σ	Δ_{Os}	2 σ
Darinskoe	0.037	1072	13790	11970	12090	16910	3893	0.12380	0.00010	0.3743	0.0004	-9.9	2.0
Duplicate	0.037	1051	13680	11340	12050	16740	4090	0.12396	0.00010	0.3702	0.0004	-5.2	2.0
Cratheús (1950)	0.054	992.6	13070	11310	11650	16110	3385	0.12426	0.00010	0.3658	0.0004	1.3	2.0
Perryville	0.091	985.6	12860	11170	11730	15810	3689	0.12470	0.00010	0.3691	0.0004	3.2	2.0
Ballinoo	0.130	793.7	10510	9234	10320	14670	3778	0.12418	0.00010	0.3637	0.0004	2.1	2.0
Kumerina	0.034	774.2	9945	8947	10540	14880	3603	0.12491	0.00010	0.3750	0.0004	0.3	2.0
Salt River	0.076	590.9	7005	7143	9740	13930	3765	0.12748	0.00010	0.4065	0.0004	1.7	2.0
Unter Mässing	0.072	415.9	4114	5170	9440	13300	4347	0.13388	0.00010	0.4875	0.0004	2.6	2.0
Wiley	0.092	194.3	1064	6949	25870	35050	4884	0.16504	0.00010	0.8845	0.0004	4.5	2.0
Cratheús (Field Museum)	0.088	252.7	2606	2444	4026	6664	3699	0.13229	0.00010	0.4676	0.0004	2.2	2.0
Pará de Minas	0.059	247.4	2540	2402	4052	6245	4021	0.13227	0.00010	0.4696	0.0004	0.5	2.0

Samples are in order of decreasing Re concentration.
Unit of weight are in g. All other concentrations are in ppb.
The uncertainties for Re and Os concentrations are ± 0.1% and the uncertainties for Ir, Ru, Pt and Pd concentrations are <2%.
Δ_{Os} is calculated by $\Delta_{Os} = 10^4 \left(^{187}Os/^{188}Os_{IIC} - (0.0956 + 0.078 \times {}^{187}Re/^{188}Os_{IIC})\right)$, where 0.0956 is the IIC initial $^{187}Os/^{188}Os$ and 0.078 is the slope of the IIC isochron.

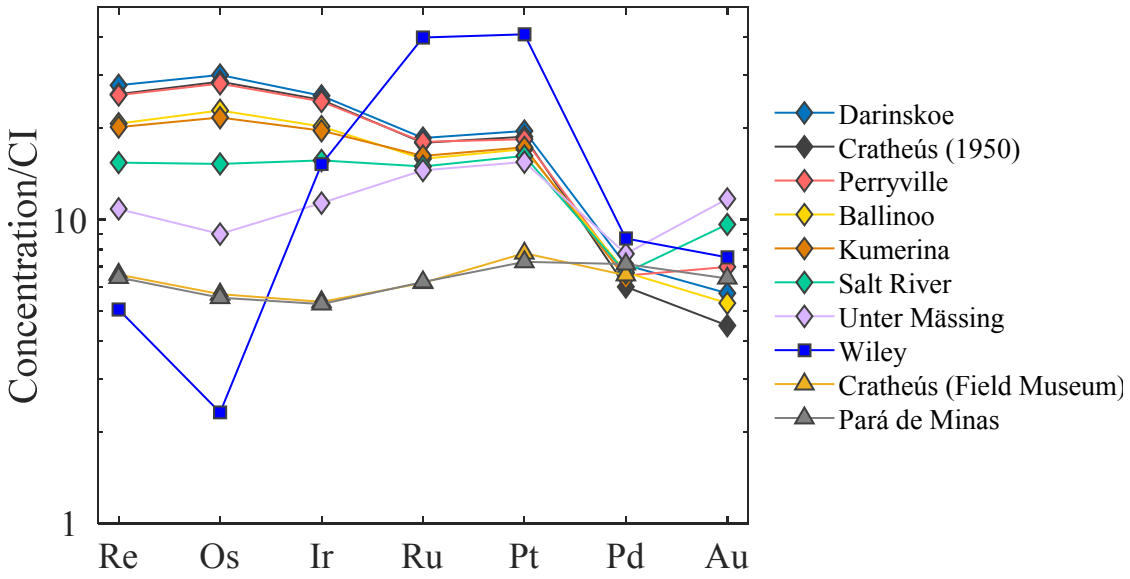

Figure 2.2 Bulk CI chondrite normalized abundance plot of HSE abundances. Data for all HSE except Au were obtained by isotope dilution for bulk samples of the IIC irons, Cratheús (Field Museum) and Pará de Minas (IVA iron). The Au data were obtained by laser ablation ICP-MS. The pattern for Wiley is considerably different from the other IIC irons and inconsistent with it being a IIC iron. Bulk composition data were normalized to Re, Os, Ir, Ru, Pt and Pd concentrations for the CI chondrite Orgueil reported by Horan et al. (2003) and Au data were normalized to average Au concentrations of CI chondrites reported by Fischer-Gödde et al. (2010).

Wiley has similar Ir, Ga, Ge, and Ni concentrations to the other IIC irons which explains its classification as a IIC iron. Yet, as noted from the LA-ICP-MS data, the bulk HSE pattern shape for Wiley strongly diverges from the other IIC irons (Fig. 2.2). Although the Re and Os concentrations of Wiley could be accounted for as a result of extensive crystal-liquid fraction from a melt that generated the other IIC irons, its Ir, Ru and Pt abundances are not consistent with this type of model. Our chemical results strongly suggest that Wiley is not a IIC iron and is unlikely to have formed from the same parental melt as the other IIC irons It should henceforth be classified as ungrouped. The isotopic data presented below are consistent with prior studies (e.g., Worsham et al., 2019) that have also arrived at this conclusion.

2.4.3. Re-Os systematics

The Re-Os isotopic data for IIC irons are provided in Table 2.2. Duplicate isotope dilution analyses of Darinskoe differ from each other beyond analytical uncertainties and plot slightly below the IIC isochron, indicative of post-crystallization Re gain or Os loss (Fig. 2.3). The Darinskoe data likely reflect minor (1-2%), relatively recent open-system behavior of Re-Os, possibly occurring on Earth.

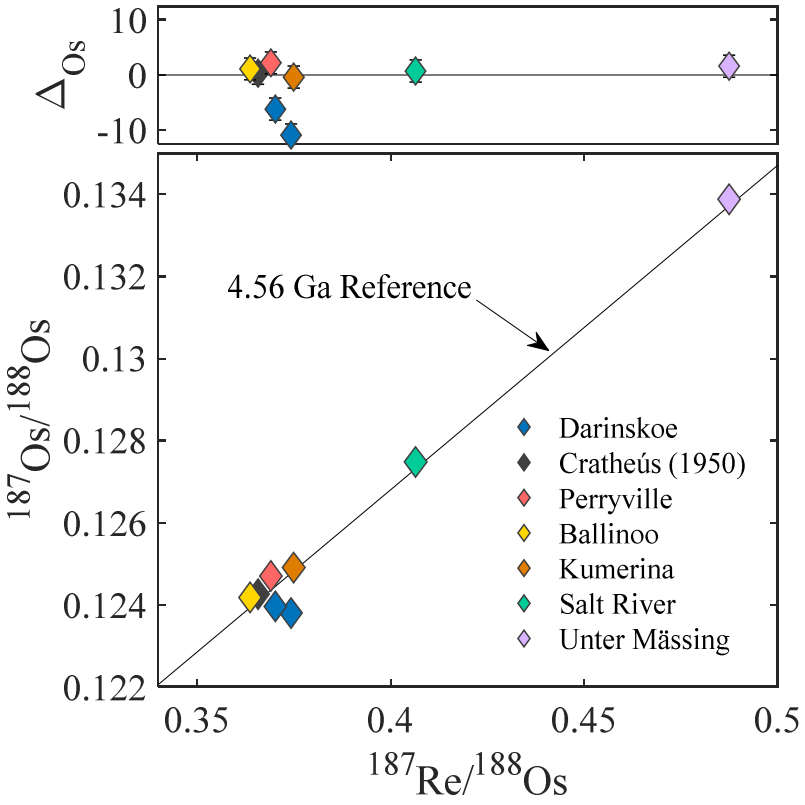

Figure 2.3 $^{187}Re/^{188}Os$ versus $^{187}Os/^{188}Os$ isochron diagram for group IIC iron meteorites. Symbols in lower figure are larger than error bars. Upper figure shows $^{187}Re/^{188}Os$ versus Δ values (parts per 10,000 deviation from the IIC isochron). The error bars represent the total analytical uncertainties (2σ). Data are shown relative to a 4.56 Ga reference isochron.

The IIC irons are characterized by a limited range in $^{187}Re/^{188}Os$ from 0.3637 to 0.4875 and $^{187}Os/^{188}Os$ from 0.1242 to 0.1339. Precision of the resulting isochron slope is consequently limited, with a regression of $^{187}Re/^{188}Os$ versus $^{187}Os/^{188}Os$ data for seven IIC

irons (excluding Darinskoe) giving an initial $^{187}Os/^{188}Os = 0.0956 \pm 0.0010$ and an age of 4538 ± 140 Myr, calculated using *ISOPLOT* (Ludwig, 2003). Nevertheless, except for Darinskoe, all IIC irons plot within uncertainties of a 4.56 Ga reference isochron, indicating closed-system behavior for these samples (Fig. 2.3).

2.4.4. Osmium isotopic compositions

The mass independent isotopic compositions of Os and Pt have been shown to be viable dosimeters of neutron capture effects resulting from long-term CRE (Fischer-Gödde et al., 2015). Osmium isotopic compositions for the IIC irons analyzed (Ballinoo, Darinskoe and Perryville) and Wiley are presented in Table 2.3. All have $\mu^{189}Os$ values ranging from -5 ± 7 to 5 ± 5, hence, no resolved variations from standards. Consequently, Mo, Ru and W isotopic data are not corrected for CRE.

Table 2.3 Osmium isotopic compositions of select IIC irons and Wiley.

Sample	n	$\mu^{189}Os$	2σ	$\mu^{190}Os$	2σ
Ballinoo	2	+3	8	-4	18
Darinskoe	2	-5	7	0	10
Perryville	3	+5	5	0	18
Wiley	3	+2	5	-1	5

n - number of analyses for each meteorite sample. The reported values are the average for each meteorite sample. Uncertainties represent the largest 2SD of the standards run during an analytical campaign.

2.4.5. Molybdenum, Ru and W isotopic compositions

Molybdenum, Ru and W isotopic compositions for Ballinoo, Darinskoe, Perryville and Wiley are reported in Tables 2.4-2.5. The $\mu^{94,95,97}$ Mo and $\mu^{183}W$ values for the averages of Ballinoo, Darinskoe and Perryville are offset to values that are higher than all other CC type iron meteorites reported by Kruijer et al. (2017), Poole et al. (2017), Bermingham et al. (2018) and Worsham et al. (2019). The new Mo isotopic data are broadly consistent

with the averages reported by Kruijer et al. (2017), Poole et al. (2017), and Worsham et al, (2019) for IIC irons and Wiley (Table S2.1). The $\mu^{94,95,97}$Mo and μ^{183}W values for Wiley are even higher than for the *bona fide* IIC irons. Average μ^{183}W values for Ballinoo and Perryville are +28 ± 3 (2SE), consistent with the +30 ± 4 value reported for Ballinoo and Kumerina by Kruijer et al. (2017). The average μ^{183}W value for Wiley is +44 ± 7, which overlaps within uncertainty with the +52 ± 3 value reported by Kruijer et al. (2017). All of the *bona fide* IIC irons analyzed for μ^{100}Ru are characterized by identical isotopic compositions, within uncertainties, averaging -99 ± 2 (2SE). This value is consistent with the -104 ± 5 average value reported for Kumerina, Perryville, and Unter Mässing by Worsham et al. (2019), and with all other CC type irons reported by Fischer-Gödde et al. (2015), Bermingham et al. (2018) and Worsham et al. (2019). The average μ^{100}Ru for Wiley is -106 ± 8, which is in agreement with the -107 ± 8 value reported by Worsham et al. (2019).

Table 2.4 Molybdenum and Ru isotopic compositions for IIC irons and Wiley.

Sample	n	μ^{92}Mo	2σ	μ^{94}Mo	2σ	μ^{95}Mo	2σ	μ^{97}Mo	2σ	n	μ^{100}Ru	2σ
Ballinoo	1	+372	34	+252	16	+159	7	+70	8	2	-99	4
Darinskoe	2	+351	47	+235	30	+149	19	+75	10	2	-100	6
Perryville	2	+345	66	+239	21	+147	15	+72	19	1	-100	6
IIC Average	5	+353	21	+240	10	+150	7	+73	5	5	-99	2
Wiley	10	+467	32	+354	12	+227	8	+117	4	4	-106	8

n - number of analyses of multiple loads onto different filaments of material from the same chemistry. The reported values are the averages for each sample. Uncertainties are 2SD ($n < 4$) or 2SE ($n \geq 4$).

Table 2.5 Tungsten isotopic compositions for IIC irons and Wiley.

Sample	n	$\mu^{182}W_{Measured}$	2σ	$\mu^{183}W_{Measured}$	2σ	$\mu^{182}W_{Corrected}$	2σ	ΔT_{CAI}	2σ
Ballinoo	1	-265	10	+34	6	-313	13	3.3	1.4
Perryville	4	-277	8	+27	1	-314	4	3.2	0.6
IIC Average	5	-274	8	+28	3	-314	9	3.2	0.7
Wiley	1	-246	8	+44	7	-308	13	3.8	1.4

n - number of analyses for each meteorite sample. The reported values are the averages for each sample. Uncertainties are the 2SD ($n < 4$) of the standards run during an analytical campaign or 2SE ($n \geq 4$) of the sample values. The $\mu^{182}W$ values are corrected for the *r*- process excess of ^{183}W.

2.5. Discussion

2.5.1. Crystallization models

Due to the predictable behavior of the HSE during magmatic processes, modeling of the HSE has proven useful in constraining the nature of the crystallization process of parent body cores (Pernicka and Wasson, 1987; Chabot and Jones, 2003; McCoy et al., 2011). Modeling HSE behavior for the IIC group can provide insight into the compositional evolution of the IIC parent body as well as the contributions of liquid-solid metal mixing during the crystallization process.

The HSE patterns of the group IIC irons are qualitatively consistent with fractional crystallization in that concentrations of Re, Os, Ir, Ru, and Pt, normally characterized by solid metal-liquid metal D values >1 (where D values are solid/liquid concentration ratios), decrease in metal as crystallization proceeds, while Pd (normally characterized by solid metal-liquid metal D values <1), increases. In this study, appropriate solid metal-liquid metal D values for the HSE were calculated using the parameterization method developed by Jones and Malvin, (1990) and advanced by Chabot et al. (2017). A comprehensive description of this method is described in the supplementary materials.

The concentrations of P and particularly S in a metallic melt can strongly affect the solid-metal liquid-metal D values of HSE during crystallization of the melts (e.g., Chabot et al., 2017). Increasing concentrations of S and P reduce the tendency of the liquid metal to host most HSE and moderately siderophile elements (MSE). Initial S and P and subsequent change in concentration must, therefore, be estimated for successful modeling of metal crystallization. However, S and P are highly incompatible elements with solid metal. As a result, they remain concentrated in the melt during fractional crystallization and leave limited direct traces of their melt concentrations in the resulting solids. Consequently, the variables for our model include the S, P, and HSE compositions of the initial melt from which the IIC irons crystallized.

As has been done for other iron meteorite groups (Hilton et al., 2019), we constrain the initial P content by dividing the average P composition of the least evolved iron meteorite in the IIC suite, Darinskoe (~0.3 wt.%) by the constant D_o value (where D_o is the solid metal-liquid metal D value in the light-element-free Fe-Ni system) for P (0.1) (Chabot et al., 2017). This suggests an initial P content of approximately 3 wt.%. An initial bulk S content can be estimated from the Ir, Ga and Ge versus Au trends (Wasson, 1999; Chabot, 2004; Goldstein et al., 2009). Gallium, Ge and Au partition are sensitive to bulk S concentrations and produce distinct non-linear trends. Thus, these elements serve as good proxies to constrain initial S. However, fractional crystallization models cannot account for Ga, Ge and Au with a single initial S content. The Ga and Ge trends are best fit by ~9 ± 1 wt.% initial S, while the Ir trend is best fit by ~0 wt.% initial S (Fig. S2.1). Due to the presence of abundant (~0.3 wt.% S) troilite nodules in some IIC irons (Buchwald, 1975), it is unlikely the IIC body had low initial S. This conclusion is supported by the fact that

the IIC group is not strongly depleted in other volatile siderophile elements (Fig. 2.1). Nevertheless, in order to better constrain initial S, we model HSE evolution with both relatively high and low initial S concentrations.

Meteorites that formed by fractional crystallization of a metallic core can represent solids directly precipitated from a liquid that they were in equilibrium with, equilibrium melt trapped in and mixed with solids, or a liquid composition preserved by entrapments in earlier formed solids (Wasson, 1999; Walker et al., 2008). In chemical evolution models, a liquid track represents the path of evolving liquid concentrations resulting from fractional crystallization. The accompanying solid track represents the path of the concentrations of equilibrium solids precipitating from the evolving liquid. A meteorite with a concentration that plots along the solid or liquid tracks can be interpreted as representing equilibrium solid or liquid, respectively. A meteorite with compositions that plots between the tracks may represent a mixture of equilibrium solids and trapped coexisting liquids.

Our detailed modeling of fractional crystallization of the IIC system begins with Re and Os, as they are the best measured HSE, and because we assume their initial concentration ratio was within the chondritic range (~0.39-0.44; Walker et al., 2002). Initial Re concentrations were estimated assuming that the first crystallizing solids had a Re concentration similar to that of the least evolved meteorite, Darinskoe. Osmium concentrations were constrained by iteration, assuming the $^{187}Re/^{188}Os$ in the initial melt was similar to chondrites. The concentrations of the rest of the HSE were constrained by varying initial concentrations to match those of Darinskoe. As noted above, although the Re-Os isotopic data for Darinskoe do not plot within uncertainties of a 4.56 Ga reference isochron, the offsets from the isochron suggest gain or loss of only 1-2% of the

concentrations of Re and Os. Such minimal open-system behavior should not affect the modeling.

Model solid and liquid evolution tracks of Re concentration versus Re/Os with IIC data are shown in Figure 2.4a-b. Two contrasting models, A and B, defined by 0 and 8 wt.% initial S, and 3 and 2 wt.% initial P, respectively, are considered. Additional models with varying S and P concentrations are presented in the supplemental materials. In both models A and B, Darinskoe is assumed to represent an equilibrium solid that formed following ~10% fractional crystallization. Since Cratheús (1950), Ballinoo, Perryville, Kumerina, and Unter Mässing plot outside of the liquid and solid tracks, model A is inconsistent with the IIC pattern. By contrast, all IIC irons plot between solid and liquid tracks, and can therefore be accounted for in model B. We conclude that the S and P content of model B best match the HSE concentration variations in the group.

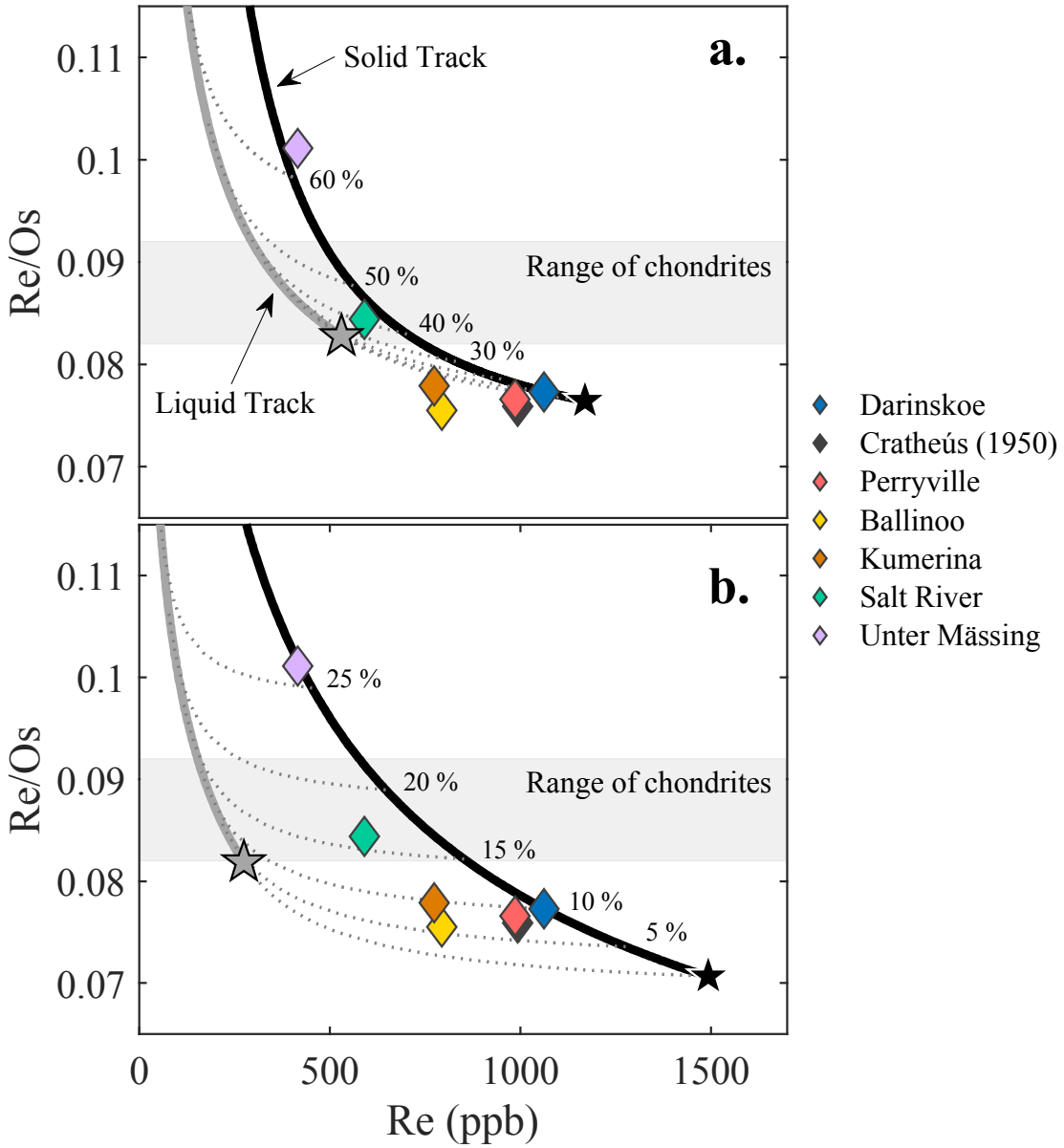

Figure 2.4a-b. (a) Fractional crystallization model for Re (ppb) versus Re/Os calculated for initial S and P concentrations of 0 and 3 wt.%, respectively. The dashed grey lines show mixing curves connecting the equilibrium solid and liquid tracks at 10% increments. **(b)** Fractional crystallization model for Re (ppb) versus Re/Os calculated for initial S and P concentrations of 8 and 2 wt.%, respectively. The dashed grey lines show mixing curves connecting the equilibrium solid and liquid tracks at 5% increments. The black line represents the solid track and the grey line represents the liquid track. The colored diamonds are the data for the IIC irons. The grey area is the range for bulk chondrites (Walker et al., 2002). The black and grey stars represent the first solid and liquid composition to form, respectively.

Given model B initial parameters, Darinskoe and Unter Mässing plot along the solid track representing equilibrium solids at 10 and 26% fractional crystallization. The modeling of the other HSE, using these initial parameters (Fig. S2.3), are in good agreement with observed concentrations of HSE (Fig. 2.5a-b), with details provided in the supplemental materials. For this model, the HSE compositions of most IIC irons reflect variable degrees of fractional crystallization, accompanied by melt trapping or mixing from the chemical evolution path. The similar HSE concentrations of Cratheús (1950) and Perryville indicate they likely crystallized at about the same point in the crystallization sequence, as is also true for Ballinoo and Kumerina.

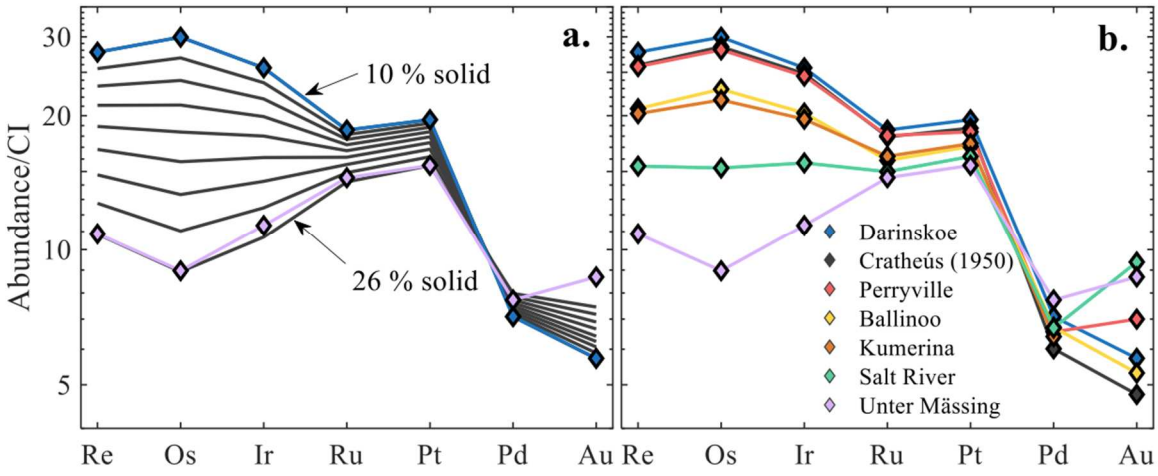

Figure 2.5 (a) CI chondrite normalized solid compositions calculated using the preferred fractional crystallization model at 2 wt.% increments. The modeled results are in good agreement with the observed patterns for the IIC irons **(b)**.

The initial melt concentrations of HSE calculated from the preferred model B for the IIC parent body core are given in Table 2.6, along with estimated initial HSE concentrations for the magmatic group IVB, IVA, and South Byron Trio (SBT) irons for comparison (Walker et al., 2008; McCoy et al., 2011; Hilton et al., 2019). Results are shown in Figure 2.6 along with a pattern representative of average carbonaceous chondrites

(Horan et al., 2003). The estimated HSE composition of the parent core for model B is approximately six times higher than the carbonaceous chondrite average. If all HSE were extracted from the silicate shell of the body into the core, these projected concentrations suggest the core was ~17% the mass of the IIC parent body.

Table 2.6. Calculated initial concentrations of HSE (in ppb) for the parameters discussed in the text.

	Re	Os	Ir	Ru	Pt	Pd	Au
IIC	280	3350	3050	4340	6070	5300	1350
IVB[a]	2800	37000	27000	27400	29500	8600	150
IVA[b]	295	3250	2700	3900	5900	4500	1320
SBT[c]	770	9400	8500	13000	16000	8400	2200[d]

[a] Data from Walker et al. (2008); [b] Data from McCoy et al. (2011); [c] Data from Hilton et al. (2019), SBT – South Byron Trio; [d] Data from McCoy et al. (2019).

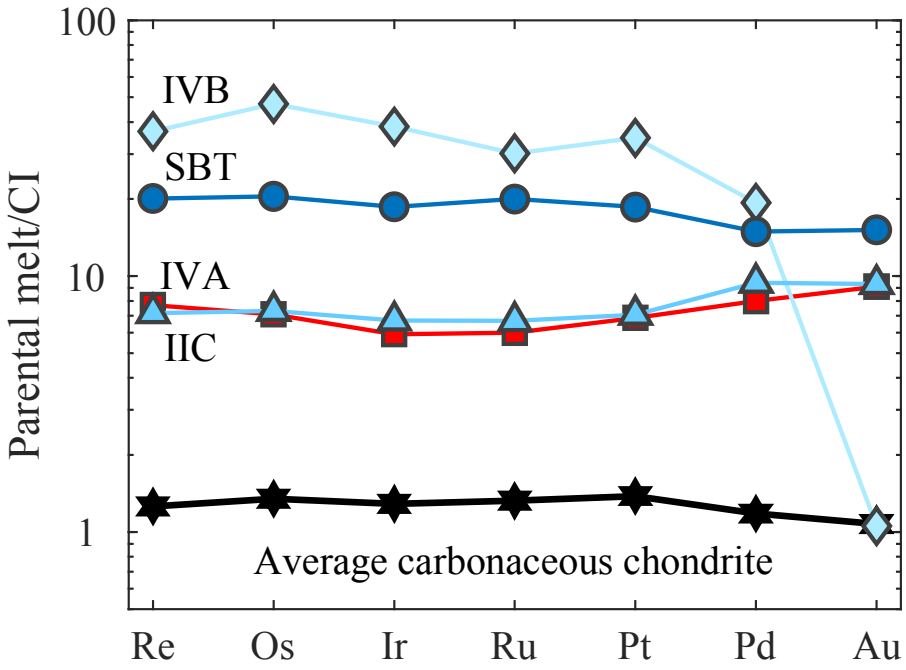

Figure 2.6. Plot of calculated parental melt HSE concentrations, normalized to Re, Os, Ir, Ru, Pt and Pd concentrations for the CI chondrite Orgueil reported by Horan et al. (2003) and Au data were normalized to average Au concentrations of CI chondrites reported by Fischer-Gödde et al. (2010). Parameter concentrations are plotted from Table 2.6. For comparison, the initial parental melt concentrations estimated by Walker et al., 2008 (IVB), McCoy et al., 2011 (IVA), and Hilton et al., 2019 (SBT) are shown.

2.5.2. Hf-W Chronology of Core Formation and Parent Body Accretion

The IIC irons can be successfully modeled by fractional crystallization from the same parental melt and thus likely reflect derivation from a single parent body core. As such, the W isotopic composition of the IIC irons can be used to constrain timing of core formation. Tungsten-182 depletions in iron meteorites have been previously used to determine the timing of parent body core formation, assuming an instantaneous core formation event (e.g., Kruijer et al., 2017). The average $\mu^{182}W$ value for the IIC body is -274 ± 8, with a $\mu^{182}W$ value corrected for excess ^{183}W of -314 ± 9 (Fig. 2.7; see supplementary materials for details). Metal-silicate Hf-W model ages are calculated relative to a solar system initial value of -349 ± 7 obtained from CAI (Kruijer et al., 2014a) and assuming a present day chondritic $\mu^{182}W$ value of -191 ± 8 (Kleine et al., 2004). The corrected value corresponds to a model metal-silicate differentiation age of 3.2 ± 0.7 Myr after CAI formation. This model differentiation age overlaps, within uncertainty, all CC type body model differentiation ages reported to date, but is the only iron meteorite group that is resolved from all NC type body model differentiation ages (Kruijer et al., 2017; Hilton et al., 2019).

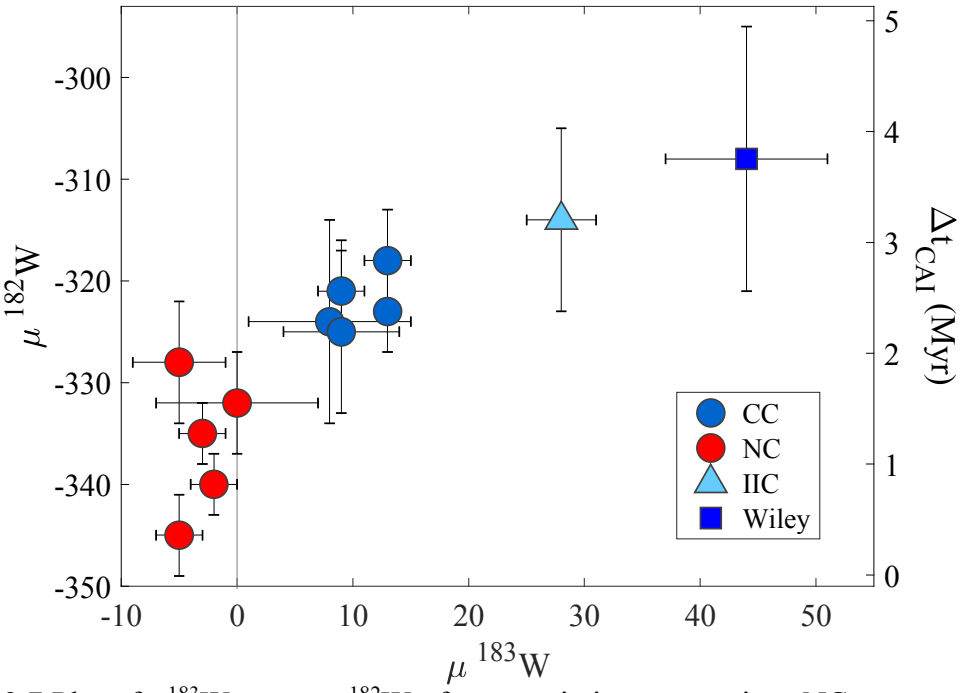

Figure 2.7 Plot of $\mu^{183}W$ versus $\mu^{182}W$ of magmatic iron meteorites. NC type meteorites include group averages of data for IC, IIAB, IIIAB IIIE and IVA irons. CC type meteorites include group averages for IID, IIF, IIIF, IVB, South Byron Trio (SBT), IIC and ungrouped iron, Wiley. Data are from this study, Kruijer et al. (2017), and Hilton et al. (2019).

The timing of core segregation can be used to assess the accretion times of meteorite parent bodies by modeling the thermal evolution of bodies heated by the decay of ^{26}Al. This model requires the knowledge of the temperature at which metal segregation and melting occurred and is dependent on the initial S concentration of iron meteorite parent bodies (Kruijer et al. 2014b). As has been done for other CC type parent bodies, an accretion age is calculated for the IIC parent body assuming single-stage core formation at a given temperature. Using a thermal model described by Kruijer et al. (2017) and Hilton et al. (2019), a parent body accretion age for the IIC group is 1.4 ± 0.5 Myr after CAI formation is obtained (see supplement for details). This age overlaps within uncertainties

with all CC and NC type iron meteorite parent bodies, with the exception of the NC type IC group, which is resolved as older (Kruijer et al., 2017; Hilton et al., 2019).

2.5.3. Parent Body Genetics

Molybdenum, Ru and W isotopic heterogeneities observed in iron meteorites have been attributed to the incorporation of different proportions of materials with distinctive nucleosynthetic signatures (*p-, r-,* and *s*-process nuclides) (e.g., Dauphas et al., 2004). These signatures can be used to assess the genetic relationships among meteorite groups and possible changes in the isotopic composition of the solar nebula with time.

In iron meteorites, Mo is useful as a tracer of the distribution of nucleosynthetic components within the solar nebula. The NC and CC types appear to define two distinct Mo *s*-process mixing lines, most easily observed in a plot of μ^{94}Mo vs. μ^{95}Mo (Budde et al., 2016; Poole et al., 2017; Worsham et al., 2017). The NC type irons show variable Mo isotopic compositions along an *s*-process mixing line, while most CC irons are indistinguishable within analytical uncertainties (Bermingham et al., 2018) and are characterized by enrichments in *r*-process Mo relative to the NC trend (Fig. 2.8). Although some carbonaceous chondrites and chondrules exhibit similar Mo isotope anomalies (Burkhardt et al., 2011; Budde et al., 2016), the IIC group exhibits the largest nucleosynthetic ^{94,95,97}Mo isotope anomalies of any iron meteorite group analyzed to date. For example, the μ^{95}Mo value for IIC irons are offset from the average CC μ^{95}Mo value by approximately 50 ppm. Further, Wiley has the largest anomalies yet reported for irons and is offset from the average CC μ^{95}Mo value by approximately 130 ppm. The IIC group and Wiley do not fall within the CC type cluster but instead plot along an apparent *s*-process mixing line with the CC type irons that is generally parallel to the NC trend. This

observation led Kruijer et al. (2017) and Poole et al. (2017) to conclude that the IIC group is of the CC type. A linear trend from the CC cluster to the IIC group and Wiley is consistent with a nebular feeding zone characterized by variable *s*-process deficits coupled with *r*- and *p*-process (e.g., μ^{92}Mo) excesses, in constant proportions, relative to NC bodies.

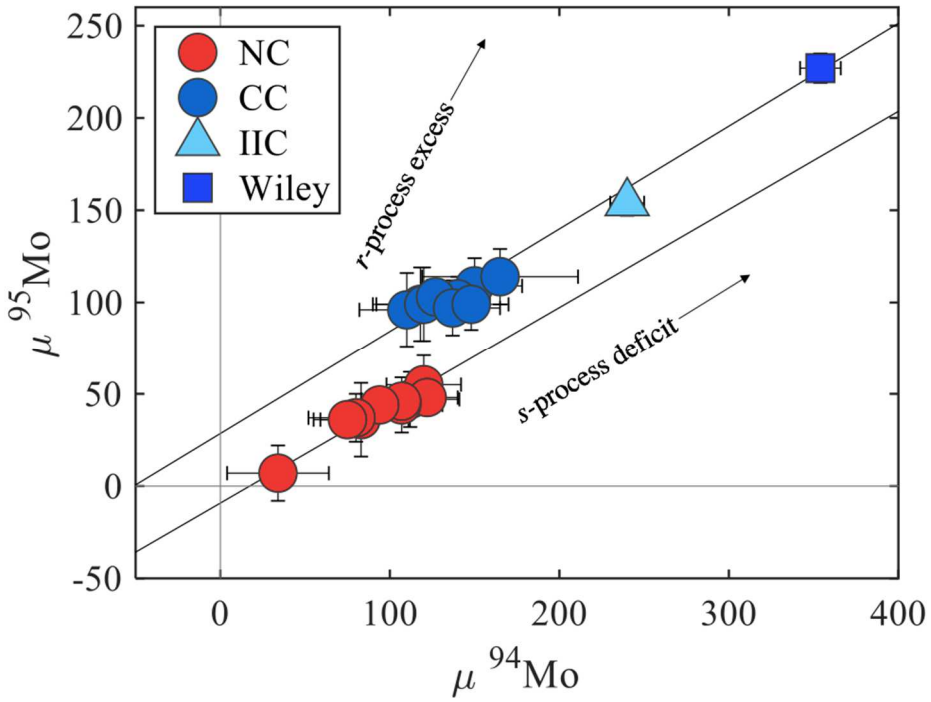

Figure 2.8 Plot of μ^{94}Mo versus μ^{95}Mo for iron meteorite groups using data from Table 2.4 and group averages reported by Bermingham et al. (2018), Worsham et al. (2019) and Hilton et al. (2019). NC type meteorites include group averages of IC, IIAB, IIIAB, IIIE, IVA and one ungrouped iron, Gebel Kamil. CC type meteorites include group averages of IID, IIF, IIIF, IVB, SBT, IIC and four ungrouped irons Wiley, Chinga, Dronino, and Tishomingo. The black lines are linear regressions calculated using *ISOPLOT*.

Isotopes of Ru add an additional dimension to examine genetic components in irons. Using a plot of ^{92}Mo vs. ^{100}Ru, Dauphas et al. (2004) noted a linear Mo-Ru relationship between iron meteorite groups and termed it the "Mo-Ru cosmic correlation." On a similar plot of μ^{97}Mo vs. ^{100}Ru, the NC type parent bodies are characterized by Mo and Ru with variable *s*- and *r*- process deficits relative to Earth (Fig. 2.9). By contrast, most of the CC

type parent bodies of irons plot within uncertainties of one another, consistent with a nebular feeding zone with homogeneously mixed ^{97}Mo and ^{100}Ru isotopic compositions (Bermingham et al., 2018; Worsham et al., 2019). The IIC irons and Wiley, however, are characterized by μ^{100}Ru values consistent with CC type irons, but greater $\mu^{94,95,97}$Mo values, as noted by Worsham et al. (2019). Consequently, they plot well off the ^{97}Mo-^{100}Ru correlation (Fig.2.9; Fig. S2.5). This is unexpected because in order to generate the linear trend on a plot of μ^{94}Mo vs. μ^{95}Mo defined by CC type irons (Fig. 2.8), the IIC group and Wiley would have to have incorporated precursor materials with variable *s*-process deficits in constant proportions. Yet the IIC irons and Wiley have no accompanying *s*-process deficits for ^{100}Ru.

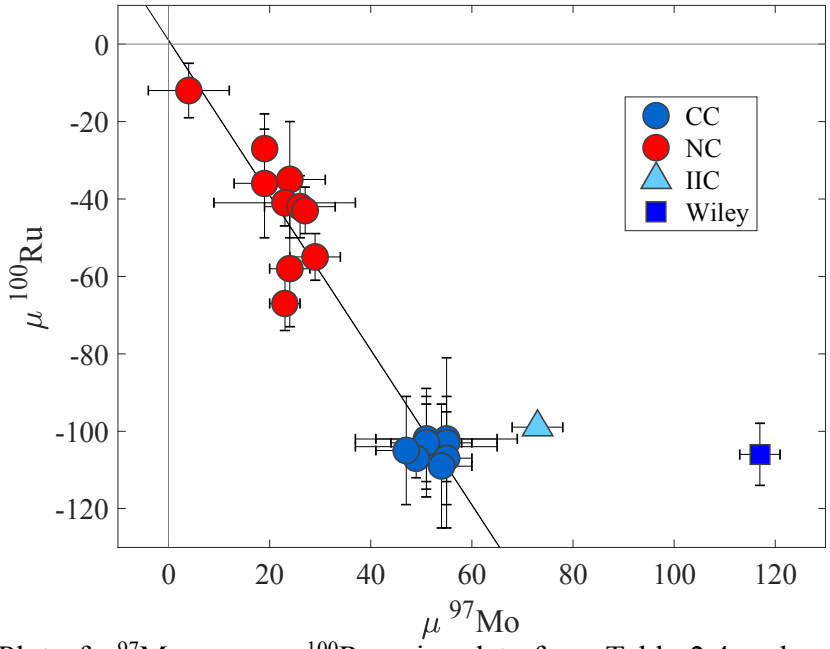

Figure 2.9 Plot of μ^{97}Mo versus μ^{100}Ru using data from Table 2.4 and group averages reported by Bermingham et al. (2018), Worsham et al. (2019) and Hilton et al. (2019). NC type meteorites include group averages of IC, IIAB, IIIAB, IIIE, IVA and one ungrouped iron, Gebel Kamil. CC type meteorites include group averages of IID, IIF, IIIF, IVB, SBT, IIC and four ungrouped irons Wiley, Chinga, Dronino, and Tishomingo. The black line is a linear regressions calculated using *ISOPLOT*.

Worsham et al. (2019) noted the NC type irons are characterized by correlated variations in μ^{i}Mo and μ^{100}Ru, yet homogeneous μ^{183}W (Fig. 2.7). Conversely, the CC type irons are characterized by correlated μ^{i}Mo and μ^{183}W, but homogeneous μ^{100}Ru (Fig. 2.9). To account for this inconsistency, Worsham et al. (2019) concluded that the isotopic homogeneity observed for μ^{183}W in the NC domain, and μ^{100}Ru in the CC domain, could be explained by assuming that each domain was initially homogeneous with respect to the isotopic compositions of all three elements. Isotopic heterogeneity might then have been introduced for some elements as a result of heating, variable volatilization, and partial loss of some elements or their presolar carrier phases. Under the more reducing conditions and higher temperatures commonly envisioned for the NC domain, Worsham et al. (2019) posited that based on 50% condensation temperatures, the extant, reduced species of Mo and Ru would have been more readily volatilized than the high refractory W, preserving ^{183}W isotopic homogeneity, but causing Mo and Ru isotopic heterogeneity. Under the more oxidizing and lower temperature conditions commonly envisioned for the CC domain, Worsham et al. (2019) proposed that Mo and W may have formed oxides more readily than Ru. Given that some oxide species of Mo and W are more volatile than reduced Ru (Fegley and Palme, 1985), this could account for the preservation of Ru isotopic homogeneity, but variable loss of ^{183}W and *s*-process isotopes of Mo. A similar model was proposed by Fischer-Gödde et al. (2015) to retain Ru isotopic homogeneity while generating Mo isotopic heterogeneity among precursor materials for carbonaceous chondrites.

2.5.4. Chemical evidence for selective volatilization processes affecting Mo, Ru and W

The putative selective volatilization processes, coupled with differences in oxidation states between CC and NC domains to create mass independent isotopic heterogeneity, as proposed by Worsham et al. (2019), might be expected to have left some evidence in the chemical compositions of the parent bodies. For example, if the Mo and W isotopic differences between NC and CC type irons are the result of variable, volatile-related losses of presolar phases bearing Mo and W in the CC domain, relative depletions in Mo and W abundances might accompany the isotopic heterogeneity of these elements in CC irons, compared with NC irons. Given that the IIC irons and Wiley are characterized by the largest Mo and W isotopic anomalies, it is also plausible that the greatest effects of loss would be most evident in these meteorites.

To assess whether Mo and W were compositionally depleted in IIC irons and Wiley relative to other CC bodies requires knowledge of the initial melt compositions of each parent body core. Although initial melt compositions can be estimated for HSE, as discussed above, the paucity of appropriate D values for other siderophile elements make their estimation more problematic. Nevertheless, during fractional crystallization, concentrations of most siderophile elements generally decrease in later crystallized solids, therefore the least evolved irons from a magmatic iron meteorite group most closely reflect the initial bulk composition of the parent body core. Consequently, we assess the depletions of W and Mo (CI-normalized), relative to other siderophile elements by considering the least chemically evolved CC irons (e.g., highest Re and Os concentrations) of each of the IIC, IVB, South Byron Trio (SBT) groups (Darinskoe, Cape of Good Hope, and Babb's

Mill (Troost's Iron), respectively), and an NC iron (Jamestown, IVA group). Depletion factors (X_i*) are calculated using Eq. 2.2;

$$\text{Eq. 2.2: } X_i^* = \left(\frac{X_i}{\frac{[X_o + X_n]}{2}} \right)$$

where X_i is the concentration of the specified element for each sample and X_o and X_n are concentrations of Os and Ir, and Ir and Pt used in the calculation for W and Mo, respectively. Osmium, Ir and Pt are chosen for the reference elements because they have 50% condensation temperatures that bracket the temperatures for W and Mo (e.g., Fig. 2.1). Darinskoe (IIC) and Wiley show no discernible depletions in Mo and W relative to the least evolved irons of other CC groups (SBT and IVB), for which comparable data are available (Fig. 2.10a-b). Of note, the IVB and SBT groups *are* characterized by depletions of W. Volatility related losses for oxidized species of W and Mo might also be expected to be accompanied by depletions in the moderately volatile siderophile elements, Ga and Ge, yet Darinskoe and Wiley are characterized by comparatively high Ga and Ge abundances, relative to most other CC irons (Fig. S2.6). The lack of discernable depletions of Mo and W does not exclude the model of Worsham et al. (2019), as the envisioned volatilized presolar components may have comprised only a small fraction of the overall abundances of Mo and W. Nevertheless, the lack of depletions also does not provide "smoking gun" evidence in favor of this type of process.

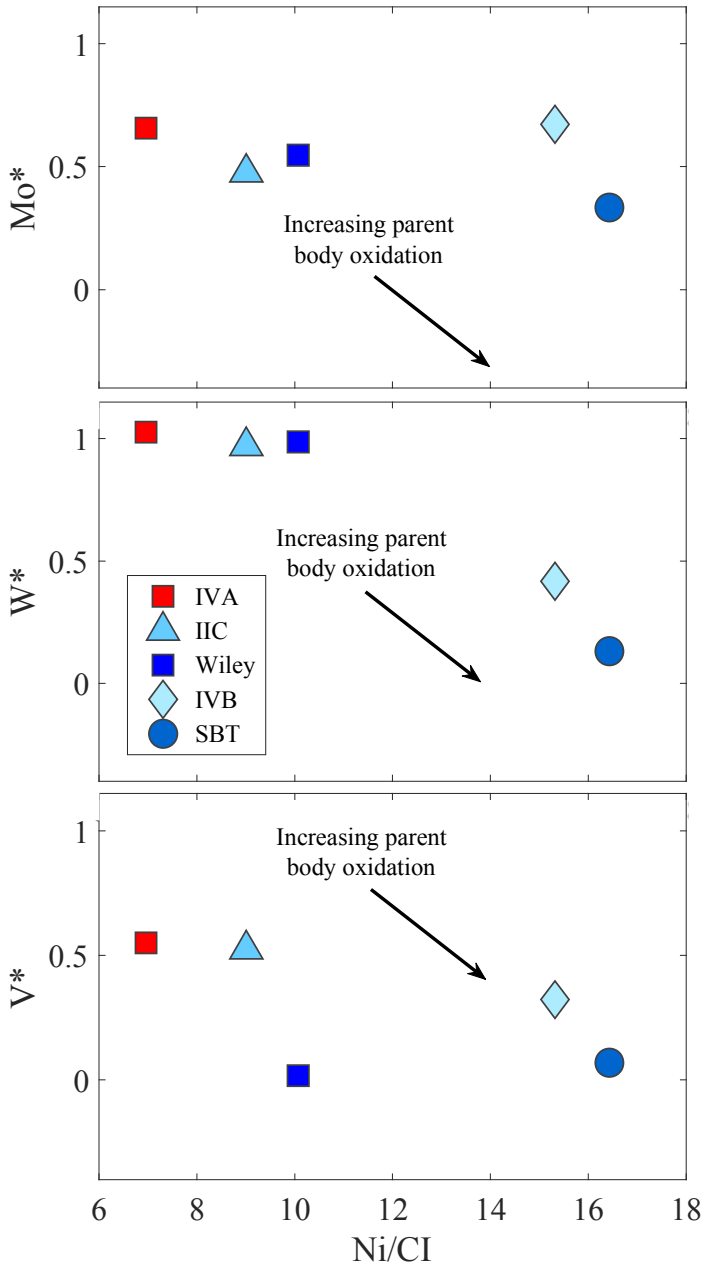

Figure 10. (a-c) Plot of relative depletions of Ni (CI-normalized) versus Mo, W and V calculated using Eq. 2 for the least evolved irons of the IVB, SBT, IIC and IVA groups and Wiley (Walker et al., 2008; Hilton et al., 2019; McCoy et al., 2011). Blue symbols are the CC bodies and red symbols are the NC bodies. The arrow is the direction that the composition of the parent body will progress with increasing oxidation. Data for the IIC and IVA (NC) group irons generally indicate a less oxidized parent body than the other CC type irons.

The next chemical characteristic of NC and CC type meteorites to consider regarding the volatilization model of Worsham et al. (2019) is oxidization state of the parent body and precursor materials. The chemical data recorded in the meteorites are mainly a reflection of oxidation conditions *during* planetesimal differentiation, which is not necessarily directly relatable to nebular conditions during the initial accretionary period, within which the selective volatilization processes presumably acted. Nevertheless, the oxidization states of planetesimals must likely, at least in part, reflect pre-accretionary conditions, and so are worthy of examination.

The oxidation states of various planetesimals at the time of primary differentiation can be broadly compared, based on several chemical criteria including initial Fe/Ni (or Ni content) of an individual iron, the concentrations of HSE estimated for the initial core melt, as well as the abundances of multivalent, redox sensitive elements such as V relative to other siderophile elements.

The average Fe/Ni (or Ni content) of an iron group is normally assumed to reflect the proportion of Fe incorporated in the silicate shell of a planetesimal relative to the core (Chabot, 2018). Thus, if Fe-Ni abundances were not fractionated in the nebula, it can be presumed that the lower the initial Fe/Ni (or higher the Ni content) of a core, the smaller the relative mass proportion of the core to the mantle. There is not a clear-cut division between NC and CC iron meteorite parent bodies with respect to Ni, although some CC groups, e.g., IVB and SBT, tend toward much higher Ni than the NC groups (Fig. S2.6). Group IIC irons, however, have approximately the same Ni content as the NC group IVA irons, with similar estimated initial Ni contents of 9.8 and 8.1 wt.%, respectively. This suggest a moderately oxidized parent body compared to, e.g., IIAB (NC) and IIIF (CC)

parent bodies, but one that was *less* oxidized than the IVB and SBT parent bodies (also CC bodies).

Wiley has a Ni content of 10.8 wt.% and is characterized by higher Ru, Pt and Pd concentrations relative to the IIC group (Fig. 2.2). This may indicate a more oxidized parent body relative to the IIC parent body, but as a single, ungrouped iron, a more precise estimation is impossible.

Similarly, core size can also potentially be constrained from the abundances of HSE estimated for the initial core melt. The higher the initial abundance, the proportionally smaller the core must be, assuming the bulk parent body was characterized by chondritic abundances of HSE. Base on this type of comparison, IVB and SBT CC type parent bodies are characterized by higher initial HSE and correspondingly smaller core sizes compared with both the IIC and IVA groups (Fig. 2.6). These data are qualitatively consistent with the conclusions derived from Ni contents, and the conclusions of Rubin et al. (2018). Although the chemical characteristics of Wiley's parent body core are unknown, the relatively high Ru, Pt and especially Pd concentrations may suggest a similar, or relatively smaller core size than the estimated IIC core. Palladium is usually not strongly fractionated in a crystallizing metallic melt, therefore the higher Pd in Wiley relative to the IIC irons suggest that the initial Pd concentration of Wiley's parental melt was modestly higher than that of the IIC initial parental melt. This assumption, in turn, suggests a slightly smaller core for the parent body.

The final indicator of oxidation state of a planetesimal to consider is the magnitude of depletions of multivalent elements, such as V, recorded in the irons. The assumption here is that under more oxidizing conditions, the multivalent elements become less siderophile

and increasingly incorporated into the silicate portions of planetesimals. Hence, abundance estimates for parental cores should be increasingly depleted relative to other siderophile elements with increased state of oxidation.

Chondritic proportions of siderophile elements with similar volatilities (e.g., Ir and Rh) provide a good reference frame for relative depletions. For example, calculated V* values (Eq. 2.2) for the least evolved irons give values of 0.32, 0.07, 0.02, 0.52 and 0.555 for the IVB, SBT, Wiley, IIC, and IVA groups, respectively (Fig. 2.10c). If these values reflect degree of oxidation, then the IIC and the NC type IVA groups formed under similar conditions. Wiley and the least evolved iron of the SBT group are characterized by comparatively lower V* values and likely formed under similar, more oxidizing conditions.

In summary, our results for the IIC parental melt composition indicate a parent body that formed under less oxidizing conditions than some other CC type bodies, such as the SBT and group IVB irons, and similar to some NC parent bodies, such as the IVA group irons (Fig. 2.6). Although the data for IIC irons do not provide evidence for a more oxidized formational environment compared to other CC type groups, the chemical data for Wiley, particularly its V* value, *do* support a somewhat more oxidized formational environment compared to NC, CC and the IIC irons, albeit the Fe/Ni for Wiley suggests a less oxidizing environment than most other CC irons.

Our new findings do not provide chemical data to support the differential volatility model of Worsham et al. (2019) to account for the genetic isotopic observations involving Ru, Mo and W in NC and CC type irons, as well as IIC irons and Wiley, but also do not invalidate the model. The presumed CC type IIC group and Wiley remain the only known irons that are characterized by combined Mo and ^{183}W isotopic compositions that

significantly differ from all other CC types. The enrichments of *p*- and *r*-process isotopes, and depletion of *s*-process isotopes in the IIC group and Wiley, relative to NC and other CC type irons, suggest that the parent bodies of these meteorites originated in a nebular reservoir that was processed in a manner that was distinct from NC and other CC type irons. As noted by Worsham et al. (2019), an alternative possibility to the thermal processing model is that of the existence of a nebular domain with genetic characteristics that differ from NC and CC type meteorites. As the genetic isotope characteristics of additional ungrouped irons become known, our knowledge of the extent of genetic diversity (or lack of additional diversity), in early-formed bodies should expand.

2.6. Conclusions

1) Siderophile element abundances of IIC iron meteorites are consistent with fractional crystallization between 10 and 26% of the bulk core, assuming a metallic melt containing 8 wt.% initial S and 2 wt.% initial P concentrations. The meteorite Wiley has chemical characteristics inconsistent with IIC irons and should be re-classified as ungrouped.
2) The IIC ^{182}Hf-^{182}W model age of 3.2 ± 0.5 Myr, following CAI formation, indicates a relatively late differentiation age for the parent body compared to NC and most other CC parent bodies. Thermal modeling suggests a parent body accretion age of 1.4 ± 0.5 after CAI formation.
3) Nucleosynthetic Mo, Ru and W isotope compositions indicate the IIC group is isotopically distinct from other known iron meteorite groups. If CC type irons, their Ru compositions support the contention that there was little Ru isotopic

heterogeneity in the CC nebular domain. By contrast, Mo and W isotopic data differ from known CC irons. This could reflect differential volatilization of Mo and W, relative to Ru in precursor materials, although the chemical data for the IIC irons and Wiley provide little supporting evidence for this.

Chapter 3: Genetics, Age and Crystallization History of Group IC Iron Meteorites

Note: For this chapter, siderophile element abundances were collected by laser ablation ICP-MS with the help of Richard Ash. I collected 100% of the highly siderophile element and Re-Os data. I conducted the chemistry and collected Mo and W isotope analysis with help from Nao Nakanishi.

3.1. Introduction

The IC iron meteorite group currently consists of 13 members that were classified based on their similar Ni, Ga and Ge concentrations (Scott, 1977). As group "I" irons, the IC suite contains minor depletions in the more volatile siderophile elements (e.g., Ga, Ge). Unlike other iron meteorite groups, the IC irons are characterized by diverse mineral textures, as well as a large range of estimated cooling rates that vary by more than 3 orders of magnitude (Scott, 1977). Their textures range from coarse octahedrites to recrystallized mineralogies (Buchwald, 1975). Two IC irons, Nocoleche and Winburg, have been classified as *anomalous* due to their unique textures (Buchwald, 1975). The IC group is believed to be magmatic in origin, suggesting the members within the group can be related to one another by fractional crystallization from the same metallic melt. The mineralogical diversity and variable cooling rates of the IC group, however, raises the question of whether these meteorites formed on the same parent body.

Meteorites that have crystallized from the same parental melt should be characterized by identical nucleosynthetic, or "genetic" isotope compositions, which are believed to have been inherited from precursor materials from which the samples formed. Mass independent isotope heterogeneity in iron meteorites is observed for numerous, isotopically diverse elements such as Mo, Ru and W (e.g., Dauphas et al., 2004; Budde et al., 2016; Poole et

al., 2017; Kruijer et al., 2017). The origin of these anomalies likely developed due to incorporation of isotopically diverse presolar materials to distinct nebular reservoirs in which iron meteorite parent bodies formed.

Previous studies have used the variations in genetic isotope characteristics to identify a dichotomy of meteorites distinguishing between non-carbonaceous (NC) and carbonaceous chondrite (CC) types (e.g., Warren, 2011). Based on the distinct Mo, Ru and W genetic characteristics observed in iron meteorites, it has been concluded by some that the NC and CC type meteorites represent distinct nebular reservoirs that were segregated, and remained isolated, by an accreting proto-Jupiter (Warren, 2011; Kruijer et al., 2017). Based on Mo isotopes, Kruijer et al. (2017) and Poole et al. (2017) concluded that the IC group is of the NC type.

The short lived ^{182}Hf-^{182}W isotope system ($t_{½}$ = 9 Myr; Vockenhuber et al., 2004) has proven to be useful in constraining the time scale of iron meteorite core formation and accretion. The IC irons are of great interest because a prior study has reported a ^{182}W/^{184}W ratio that overlaps with the initial ^{182}W/^{184}W ratio that has been determined for calcium aluminum rich inclusion (CAI) (Kruijer et al., 2017), suggesting parent body accretion and differentiation occurred very soon after initial formation of solids in the protosolar nebula. The IC group therefore, may be the earliest formed differentiated body for which we have samples. Chemical and isotopic analysis of the IC group, therefore, can potentially provide new insights into the earliest stages of solar system evolution.

One goal of this study is to tighten constraints on the IC group segregation and accretion age by analyzing multiple IC samples for ^{182}Hf-^{182}W systematics in order to reduce the statistical uncertainty in the model age of this group. Additionally, modeling the

siderophile element compositions of the IC group will provide insight as to whether all or some IC irons can be related by fractional crystallization, and if the projected parent body composition was chemically distinct relative to later formed NC and CC type groups. Molybdenum isotopic compositions will be used to assess whether meteorites classified as IC were derived from the same genetic reservoir, with particular interest in assessing whether the anomalous meteorites were formed from the same genetic mix.

3.2. Samples

In all, eleven of the thirteen recognized IC iron meteorites were obtained for this study. Eight meteorite samples were obtained from the Smithsonian Institution, National Museum of Natural History, USA: Arispe (USNM 2638), Chihuahua City (USNM 853), Mount Dooling (USNM 5713), Nocoleche (USNM 2967), St. Francois County (USNM 130), Santa Rosa (USNM 3046), Union County (USNM 1170), and Winburg (USNM 6390). NWA 2743 was obtained from Arizona Skies Meteorites, Flagstaff, Arizona, Bendego was obtained from the Museu Nacional/UFRJ, Brazil, and Etosha was obtained from the UCLA Meteorite Collection.

3.3. Analytical Methods

3.3.1. Laser Ablation ICP-MS

Ten samples were cut into approximately 100 mg pieces using a water-cooled diamond blade saw. Each piece was polished with carborundum paper and sonicated in ethanol to remove any saw blade contamination. Siderophile element concentrations were obtained for polished surfaces by laser ablation using a *New Wave* UP213 ultraviolet laser coupled to a *Thermo-Finnigan Element 2* inductively coupled plasma mass spectrometer (ICP-MS),

with details of the instrumentation parameters provided in Chapter 2. All data were processed using *LAMTRACE* (Rusk, 2009) using the previously measured concentrations of the iron meteorites Hoba, Filomena and Coahuila. Initially, Fe was used as an internal standard for the IC group using accepted values in the literature, then all concentrations were recalculated to force Fe, Ni, and Co concentrations to sum to 100%.

3.3.2. ^{187}Re-^{187}Os and siderophile element analysis

The chemical-separation techniques used in this study have been previously published (e.g., McCoy et al., 2011). Bulk sample isotope dilution measurements of the highly siderophile elements (HSE) Re, Os, Ir, Ru, Pt and Pd were performed on 0.02-0.28 g pieces of polished chunks using combined ICP-MS and thermal ionization mass spectrometry (TIMS). Each sample was spiked with appropriate amounts of separate ^{185}Re-^{190}Os and ^{191}Ir-^{99}Ru-^{194}Pt-^{105}Pd mixed spikes for isotope dilution. Sample and spike mixtures were sealed and digested in *Pyrex*™ Carius tubes at 230˚C for ≥24 hours along with 5 mL of high purity concentrated HNO_3 and 2.5 mL of high purity concentrated HCl. After opening the tubes, Os was immediately extracted using a carbon tetrachloride method (Cohen and Waters, 1996) and further purified by microdistillation (Birck et al., 1997). Approximately 100-200 ng of purified Os was loaded onto an outgassed Pt filament along with Ba hydroxide activator and analyzed as OsO_3^- by TIMS using standard techniques. Osmium isotope dilution data were corrected for natural and instrumental mass fractionation by normalizing ^{190}Os/^{188}Os to 3.08271 (Allègre and Luck, 1980).

Rhenium. Ir, Ru, Pt and Pd were separated and purified from the remaining aqueous phase using anion exchange columns (Rehkamper and Halliday, 1997) with 0.2 mL of 100-

200 mesh resin. Each sample was loaded into a column with 0.8 M HNO_3, then eluted with 12 mL 6 M HNO_3 for Re and Ru, 12 mL concentrated HNO_3 for Ir and Pt, and 15 mL concentrated HCl for Pd. Rhenium and Ru aliquots were further purified using a smaller version of the primary anion column. The HSE cuts were dried, taken up in 0.8 M HNO_3, and were analyzed using a *Thermo Neptune Plus* multi-collector ICP-MS.

Approximately 1-7 g pieces of seven IC irons were dissolved in 50-100 mL 8 M HCl at 140 ˚C for 48 h in Teflon® beakers for high precision measurements of Mo and W. The chemical separation and purification procedures have been previously published (Nagai and Yokoyama, 2014; Worsham et al., 2016) and briefly described here. Results of isotopic compositions in this study are reported using the μ notation (e.g., Mo):

$$\text{Eq. 3.1: } \mu^{97}\text{Mo} = \left(\frac{\frac{97}{96}\text{Mo}_{\text{sample}}}{\frac{97}{96}\text{Mo}_{\text{standard}}} - 1 \right) * 10^6$$

One aliquot for W and Mo was dried down and dissolved in 0.4 M HCl – 0.5 M HF and loaded onto a primary anion column with 2 mL Eichrom 1 x 8 200-400 mesh resin. Tungsten was eluted with 9 M HCl – 1 M HF and Mo was eluted with 6 M HNO3 – 3 M HF. The W aliquot was dried, re-dissolved in 0.4 M HCl – 0.5 M HF and loaded onto a smaller version of the primary anion column for further purification. Tungsten was eluted with 9 M HCl-3 M HF, dried, dissolved in 1 M HCl – 0.01 M HF and approximately 1000 ng W were loaded onto an outgassed single Re filament with 1 µL of 5 µg/µL La-5 µg/µL Gd activator solution. Tungsten was analyzed as WO_3^- by TIMS using techniques by Archer et al. (2017). Mass interferences from ReO_3^- were monitored and corrected for. Tungsten isotopic data were corrected for natural and instrumental mass fractionation by normalizing $^{186}W/^{184}W$ to 0.92767 (Völkening et al., 1991). The external (2σ)

reproducibility of repeated analyses of the terrestrial laboratory standard analyzed were ± 5 ppm and ± 6 ppm for $\mu^{182}W$ and $\mu^{183}W$, respectively.

From the primary column, Mo was dried, dissolved in 6 M HCl, loaded onto a smaller anion column with ~0.3 mL AG 1x8 200-400 mesh resin and eluted with 1 M HCl. This smaller anion column elution was repeated twice. Aliquots were dried, re-dissolved in 6 M HCl and approximately 1000 ng Mo were loaded onto outgassed Re filaments along with ~2 µL of 5 µg/µL $La(NO_3)_3$ activator solution. A double filament assembly was used with the same amount of $La(NO_3)_3$ activator on the second filament. Molybdenum was analyzed as MoO_3^- by TIMS. To correct for O interferences, the $^{100}Mo^{18}O^{16}O_2^-$ species was measured using a 10^{13} Ω resistor amplifier. Molybdenum isotopic data were corrected for natural and instrumental mass fractionation by normalizing $^{98}Mo/^{96}Mo$ to 1.453171 (Lu and Masuda, 1994). The maximum external (2σ) reproducibility of repeated analyses of the terrestrial laboratory standard analyzed were ± 17 ppm, ± 15 ppm, and ± 8 ppm for $\mu^{94}Mo$, $\mu^{95}Mo$, and $\mu^{97}Mo$, respectively.

3.3.3. Cosmic ray exposure corrections

Molybdenum and W isotopic compositions are subject to modification by cosmic ray exposure. Increasingly greater CRE will shift Mo and ^{182}W isotopic compositions toward increasingly negative values. The magnitude of isotopic shift for a given sample depends on the duration of cosmogenic effects and location within the meteoroid (i.e., shielding). Molybdenum and ^{182}W isotopic variations within an iron meteorite group are highly plausible if these cosmogenic effects are left uncorrected**.** Although CRE is not monitored in this study, Kruijer et al. (2017) has shown that some IC irons (Arispe and

Bendego) have been modified by CRE and will require corrections. As such, the preliminary isotopic compositions reported here will require re-examination following the appropriate corrections.

3.4. Results

3.4.1. Molybdenum and W isotopic compositions

Molybdenum and W isotope data that are uncorrected for CRE for Arispe, Bendego, Chihuahua City, Nocoleche and Winburg are reported in Tables 3.1-3.2. The Mo data for Arispe, Bendego and Chihuahua City are in good agreement with the data reported by Burkhardt et al. (2011), Poole et al. (2017), Kruijer et al. (2017) and Worsham et al. (2019) (Table S3.1). Arispe, Bendego and Chihuahua City exhibit uniform $\mu^{94,95,97}$Mo values. The new Mo isotopic data for the anomalous IC irons, Nocoleche and Winburg, are distinctly higher for μ^{94}Mo and μ^{95}Mo and lower for μ^{97}Mo.

Table 3.1 Molybdenum isotopic compositions for IC irons.

Sample	n	μ^{94}Mo	2σ	μ^{95}Mo	2σ	μ^{97}Mo	2σ
Arispe	1	+78	10	+23	6	+22	6
Bendego	3	+85	3	+22	6	+12	3
Chihuahua City	1	+72	17	+27	8	+15	7
Nocoleche (anomalous)	1	+138	17	+35	8	-1	7
Winburg (anomalous)	1	+130	17	+46	9	-22	7

n - number of analyses of multiple loads onto different filaments of material from the same chemistry. The reported values are the averages for each sample. Uncertainties are 2SD ($n < 4$) or 2SE ($n \geq 4$).

Table 3.2 Tungsten isotopic compositions for IC irons.

Sample	n	$\mu^{182}W_{Measured}$	2σ	$\mu^{183}W_{Measured}$	2σ	$\mu^{182}W_{Corrected}$	2σ	ΔT_{CAI}	2σ
Arispe	1	-382	5	+1	5	-384	9	-2.6	0.7
Bendego	1	-365	5	-9	5	-353	9	-0.3	0.7
Chihuahua City	1	-320	5	-1	5	-319	9	2.7	0.7
Nocoleche (anomalous)	1	-246	5	+1	5	-305	9	4.2	0.8
Winburg (anomalous)	1	-309	5	-3	5	-288	9	6.2	0.7

n - number of analyses for each meteorite sample. The reported values are the averages for each sample. Uncertainties are the 2SD ($n < 4$) of the standards run during an analytical campaign or 2SE ($n \geq 4$) of the sample values. The μ^{182}W values are corrected for the *r*- process excess of ^{183}W.

Cosmic ray exposure uncorrected μ^{183}W values range from -9 ± 5 to +3 ± 5 for the samples analyzed here. Bendego is the only IC iron analyzed that is resolved from the terrestrial laboratory standard. The measured μ^{182}W values for Arispe, Bendego, Chihuahua City, Nocoleche and Winburg are not within uncertainty of each other. Arispe and Bendego have μ^{182}W values that are below the initial μ^{182}W value determined for CAI of -349 ± 7 (Kruijer et al., 2014b) (Fig. 3.1). Chihuahua City, Nocoleche and Winburg have μ^{182}W values that are higher than that of the initial value for CAI. The offsets for Chihuahua City, Nocoleche and Winburg could not be the result of cosmogenic effects as CRE corrections would shift their W isotopic compositions toward more positive values.

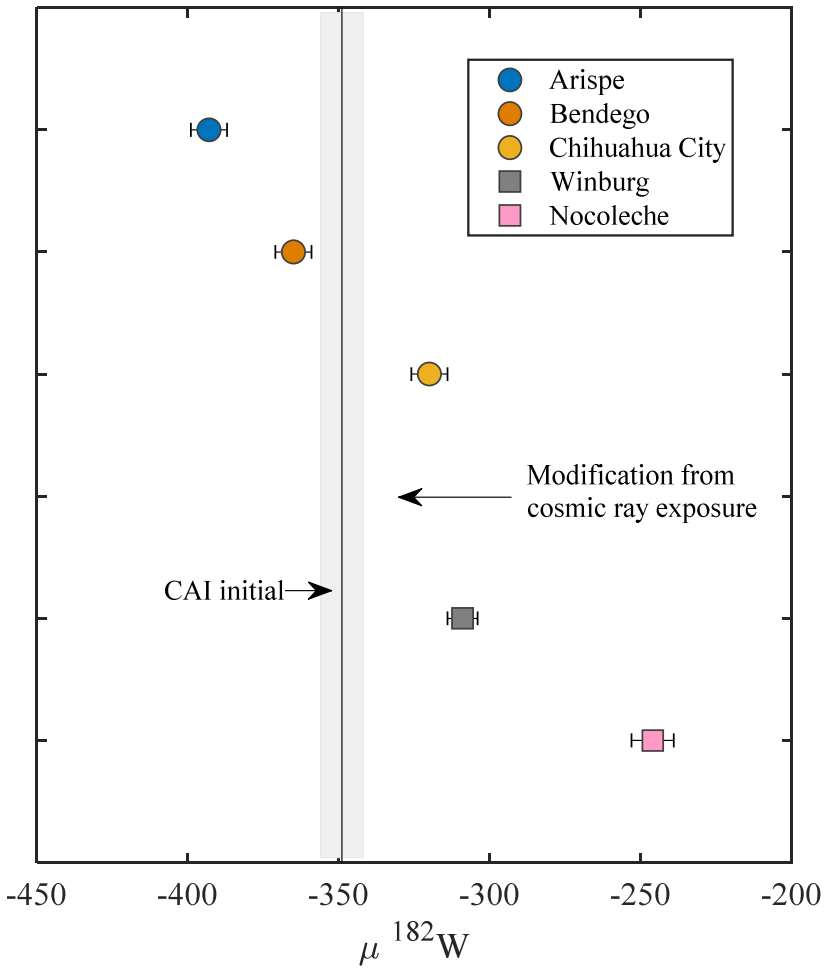

Figure 3.1 Cosmic ray exposure uncorrected $\mu^{182}W$ variation for the IC group. Error bars reflect the 2SD of repeated analysis of the terrestrial standard during the respective analytical campaign. The solid black line is the initial $\mu^{182}W$ value determined for CAI of -349 ± 7 (Kruijer et al., 2014b).

3.4.2. Composition analysis by laser ablation ICP-MS

The IC irons are characterized by a large range of diverse metallographic structures. Most IC irons contain abundant phosphide and sulfide minerals, as well as chromite and cohenite [$(Fe, Ni, Co)_3C$] while others exhibit anomalous structures (Buchwald, 1975). Average elemental concentrations obtained by LA-ICP-MS and 2σ variations for multiple lines of analysis are given in Table 3.3. The absolute abundance heterogeneity observed for some elements can largely be related to heterogeneities reflected by the phases in which

the laser beam advanced along tracks that encountered the mineral phases listed above. Siderophile elements are typically in lower abundances in these phases compared to average metal, so the siderophile element concentrations averaged along an ablation track that intersected one of these phases tended to be lower than the tracks that did not intersect a mineral phase. For the purposes here, the scale of the sample heterogeneity is not sufficient to affect the conclusions below which are largely based on large difference in relative HSE abundances within the IC group.

Bulk composition data, normalized to CI chondrites, are characterized by broadly similar patterns for most IC irons (Fig. 3.2). Consistent with their group I classification, there is a minor depletion in volatile siderophile elements, such as Ga and Ge, relative to the more refractory siderophile elements. The refractory elements in the IC irons are generally in chondritic proportions while the concentrations of Re, Os and Ir are modestly fractionated and range over two orders of magnitude (Fig. 3.2). These irons exhibit major depletions in the multivalent elements V, Cr, P and Zn relative to siderophile elements of similar volatility. Of note, the siderophile element abundance patterns for Nocoleche and Winburg are generally similar to those of the non-anomalous IC irons.

Table 3.3 Average elemental concentrations obtained by LA-ICP-MS. Group IC irons are listed from left to right in order of decreasing Re concentration.

	Arispe	Union County	Mount Dooling	Chihuahua City	Santa Rosa	Bendego
Re	0.8 ± 0.2	0.16 ± 0.06	0.1 ± 0.2	0.03 ± 0.04	0.01 ± 0.02	0.01 ± 0.01
Os	6.9 ± 0.9	1.3 ± 0.5	0.4 ± 0.6	0.07 ± 0.06	0.02 ± 0.03	0.06 ± 0.06
W	2.0 ± 0.3	2.2 ± 0.8	2.1 ± 1.4	0.6 ± 0.4	0.9 ± 0.1	1.5 ± 0.4
Ir	10.0 ± 1.4	2.8 ± 0.9	1.1 ± 0.2	0.13 ± 0.05	0.06 ± 0.03	0.20 ± 0.03
Mo	7.4 ± 3.1	7.7 ± 1.8	11.3 ± 1.5	8.73 ± 2.07	7.9 ± 5.7	6.3 ± 2.5
Ru	14.0 ± 2.2	14.8 ± 2.1	12.5 ± 1.5	4.1 ± 0.2	3.7 ± 1.8	7.73 ± 1.08
V	3.8 ± 1.0	3.4 ± 9.2	b.d.	0.7 ± 1.0	b.d.	1.8 ± 1.0
Pt	19.3 ± 1.6	21.3 ± 6.7	16.6 ± 0.5	4.7 ± 0.9	5.0 ± 2.3	12.0 ± 0.7
Rh	1.9 ± 0.2	2.1 ± 0.5	1.9 ± 0.2	1.6 ± 0.2	1.4 ± 0.4	2.0 ± 0.3
Ni	6.2 ± 0.7	5.7 ± 0.7	5.7 ± 1.2	6.6 ± 0.4	6.3 ± 1.6	5.6 ± 0.7
Co	0.47 ± 0.02	0.48 ± 0.05	0.46 ± 0.04	0.49 ± 0.02	0.49 ± 0.01	0.48 ± 0.02
Fe[a]	93.0	93.4	93.0	92.9	92.9	93.1
Pd	2.6 ± 0.5	1.8 ± 0.3	1.9 ± 0.1	2.1 ± 0.7	2.4 ± 1.3	2.6 ± 0.3
Cr	84 ± 121	52.0 ± 4.2	61 ± 20	86 ± 39	115 ± 59	44 ± 80
P	0.2 ± 0.2	0.3 ± 0.2	0.5 ± 0.7	0.9 ± 0.3	1.0 ± 2.2	0.13 ± 0.02
As	5.6 ± 2.2	4.3 ± 0.8	3.8 ± 0.2	10.8 ± 3.9	9.0 ± 4.8	9.0 ± 2.4
Au	0.6 ± 0.1	0.5 ± 0.2	0.3 ± 0.1	0.56 ± 0.09	0.4 ± 0.1	0.4 ± 0.1
Ga	50.9 ± 3.9	56.4 ± 7.2	53.7 ± 4.3	50.5 ± 2.5	48.7 ± 3.9	54.4 ± 2.6
Ge	235 ± 15	262 ± 69	230 ± 14	207.6 ± 3.4	193.5 ± 55.8	230.5 ± 8.2
Zn	1.3 ± 0.6	4.3 ± 12.7	1.3 ± 1.4	1.2 ± 0.3	1.36 ± 0.02	1.3 ± 0.8
n	*4*	*6*	*3*	*3*	*3*	*3*

	St Francois County	NWA 2743	Nocoleche (anomalous)	Winburg (anomalous)
Re	0.01 ± 0.02	0.01 ± 0.02	0.8 ± 0.1	0.08 ± 0.07
Os	0.03 ± 0.07	0.05 ± 0.03	7.8 ± 0.5	0.36 ± 0.08
W	1.21 ± 0.07	0.9 ± 0.1	1.8 ± 0.5	1.1 ± 0.2
Ir	0.14 ± 0.07	0.15 ± 0.07	8.3 ± 0.8	1.1 ± 0.1
Mo	6.3 ± 2.9	9.0 ± 3.0	6.0 ± 1.3	7.3 ± 2.5
Ru	6.5 ± 2.2	4.6 ± 0.8	10.9 ± 0.8	7.4 ± 1.9
V	b.d.	b.d.	b.d.	b.d.
Pt	10.1 ± 2.4	6.0 ± 0.6	16.9 ± 1.8	9.1 ± 1.0
Rh	1.5 ± 0.2	1.6 ± 0.2	1.6 ± 0.2	1.8 ± 0.3
Ni	4.8 ± 1.6	6.12 ± 1.03	5.8 ± 0.1	7.6 ± 2.7
Co	0.53 ± 0.04	0.50 ± 0.05	0.46 ± 0.02	0.46 ± 0.07
Fe[a]	92.8	92.8	93.1	92.6
Pd	1.9 ± 1.5	2.4 ± 0.5	1.8 ± 0.4	3.2 ± 0.5
Cr	36 ± 29	50 ± 51	109 ± 211	51 ± 37
P	0.5 ± 0.6	0.3 ± 0.3	0.3 ± 0.2	0.3 ± 0.4
As	6.6 ± 0.7	6.4 ± 1.3	4.0 ± 1.3	8.8 ± 3.0
Au	0.68 ± 0.04	0.7 ± 0.1	0.4 ± 0.1	0.8 ± 0.1
Ga	46.3 ± 3.3	47.6 ± 3.9	47.0 ± 0.8	50.5 ± 4.2
Ge	220.5 ± 10.7	201.8 ± 14.4	136.7 ± 5.0	217 ± 41
Zn	1.0 ± 0.9	1.7 ± 1.4	2.0 ± 0.6	2.7 ± 3.4
n	*3*	*5*	*3*	*3*

Nickel, Co, Fe and P concentrations reported in wt.%, all others reported in ppm.
The 2σ values reported were determined from the reproducibility of the number of lines measured (*n*) for each sample.
b.d. Concentration data below detection limits.

[a] Fe data were used as an internal standard

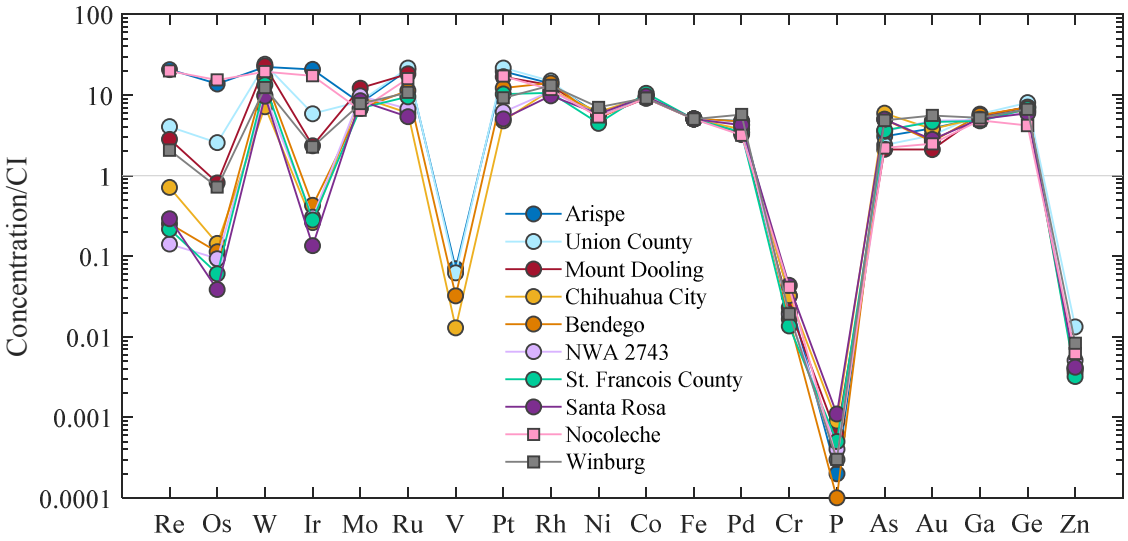

Figure 3.2 CI chondrite normalized abundances of siderophile elements for the IC irons. Elements are in order of decreasing 50 % condensation temperatures from left to right.

3.4.3. ^{187}Re-^{187}Os and highly siderophile element concentrations

Rhenium-Os isotopic, and bulk HSE concentration data for the IC iron meteorites and Nocoleche are reported in Table 3.4. NWA 2743 was processed twice to assess sample heterogeneity and reproducibility. Duplicate absolute concentrations of HSE in NWA 2743 yield percentage differences of ~5% for Re, Os, Ru and Pt, and ~25% for Ir and Pd. These differences are likely due to the size of sample digested. Duplicate ^{187}Re/^{188}Os and ^{187}Os/^{188}Os of this meteorite differ from each other beyond analytical uncertainties but suggest reproducibility of 4.1% and 0.4%, respectively. Duplicate analyses of NWA 2743 both fall along a 4.56 Ga reference isochron, consistent with closed-system isotopic and elemental systematics. The HSE concentrations of the IC group obtained by isotope dilution are on average within 0.2-10% of values obtained by LA-ICP-MS, but some deviations range up to 40%.

Table 3.4 Osmium isotopic and HSE composition data, obtained by isotope dilution, for the IC irons.

Sample	Wt.	Re	Os	Ir	Ru	Pt	Pd	$^{187}Os/^{188}Os$	2σ	$^{187}Re/^{188}Os$	2σ	Δ_{Os}	2 σ
Arispe	0.018	773.8	6737	9566	13220	18750	2897	0.13914	0.00010	0.5543	0.0004	-0.6	2
Union County	0.026	145.6	1022	2270	13190	18710	1705	0.15017	0.00010	0.6883	0.0004	-0.2	2
Mount Dooling	0.190	71.52	368.0	1198	11910	17380	2118	0.17170	0.00010	0.9418	0.0004	2.1	2
Bendego	0.056	15.47	139.7	291	10776	15340	2269	0.13649	0.00010	0.5343	0.0004	-1.7	2
Chihuahua City	0.223	9.774	89.27	125	3773	5174	3185	0.13464	0.00010	0.5280	0.0004	-3.1	2
NWA 2743	0.019	10.23	78.72	136	4813	6048	2665	0.14416	0.00010	0.6275	0.0004	-1.4	2
Duplicate	0.206	9.437	75.63	107	4583	6264	3267	0.14352	0.00010	0.6025	0.0004	0.7	2
St. Francois County	0.206	5.817	39.64	92	8195	11320	3140	0.15255	0.00010	0.7095	0.0004	1.3	2
Santa Rosa	0.278	4.671	35.68	46	4074	6030	3905	0.14633	0.00010	0.6323	0.0004	0.4	2
Nocoleche (anomalous)	0.020	657.4	7329	7568	11220	16280	2033	0.12942	0.00010	0.4323	0.0004	-0.7	2
Winburg (anomalous)	0.020	69.63	375.7	972	6539	8707	2892	0.16490	0.00010	0.8959	0.0004	-1.9	2

Samples are in order of decreasing Re concentration.
Unit of weight are in g. All other concentrations are in ppb.
The uncertainties for Re and Os concentrations are ± 0.1% (2SD) and the uncertainties for Ir, Ru, Pt and Pd concentrations are <2% (2SD).

The moderate fractionation of Re from Os during crystallization of the IC group results in a modest range in $^{187}Re/^{188}Os$ from 0.5280 (Chihuahua City) to 0.9418 (Mount Dooling), and a corresponding range in $^{187}Os/^{188}Os$ from 0.13464 to 0.17170. Two samples, Mount Dooling and Chihuahua City, do not plot within uncertainties of the IC isochron, indicative of minor post-crystallization Re gain or Os loss (Fig. 3.3). A regression of $^{187}Re/^{188}Os$ versus $^{187}Os/^{188}Os$ data for the IC irons (including duplicates but excluding Mount Dooling and Chihuahua City) gives an initial $^{187}Os/^{188}Os = 0.0962 \pm 0.0054$ and an imprecise age of 4490 ± 450 Myr, calculated using *ISOPLOT* (Ludwig, 2003), consistent with other iron meteorite groups (Walker et al., 2008; McCoy et al., 2011).

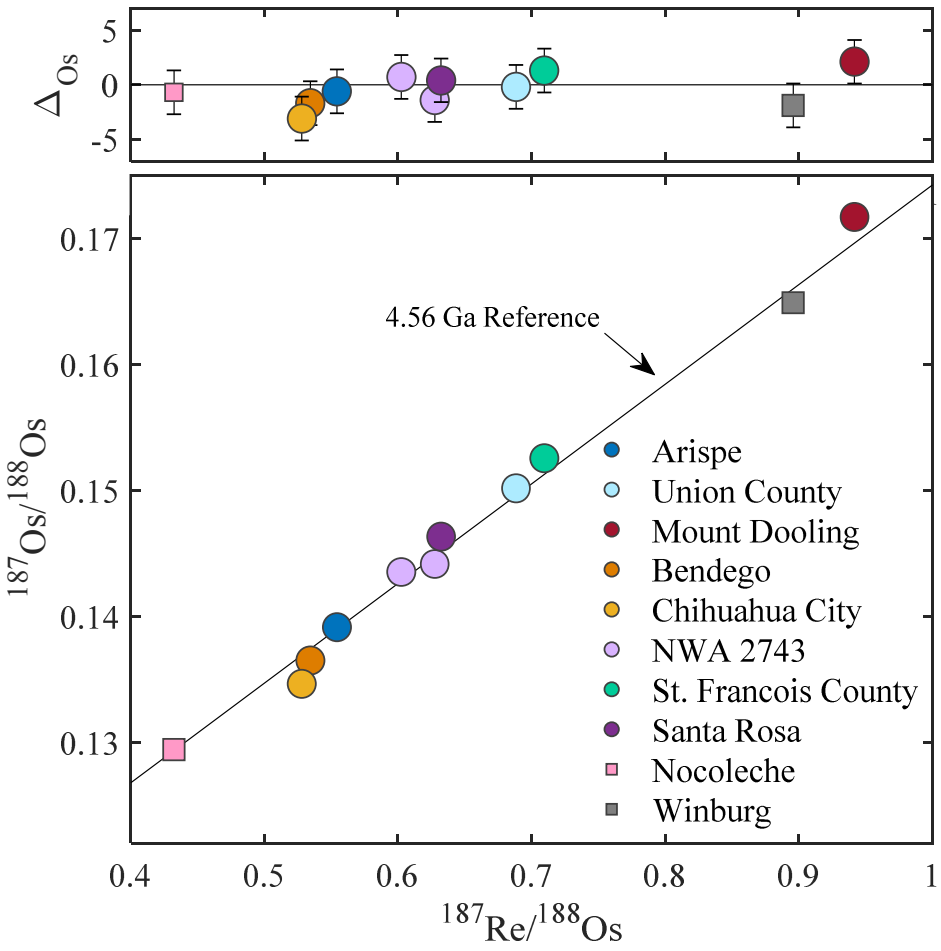

Figure 3.3 $^{187}Re/^{188}Os$ versus $^{187}Os/^{188}Os$ for group IC iron meteorites. Symbols in lower figure are larger than error bars. Upper figure shows $^{187}Re/^{188}Os$ versus Δ values (parts per 10,000 deviation from the IC isochron). The error bars represent the total analytical uncertainties (2σ).

Chondrite normalized HSE patterns of the IC irons are characterized by similar features (Fig. 3.4). The HSE concentrations of the IC irons, with the exception of Nocoleche, are fractionated relative to chondritic abundances. Nocoleche is characterized by suprachondritic absolute Re, Os, Ir, Ru and Pt abundances that are in approximately chondritic relative abundances, but with a substantial depletion in Pd. The IC group is believed to be magmatic in origin, but unlike other magmatic iron groups, the HSE patterns

for some meteorites cross. For example, Santa Rosa has the lowest concentrations of Re, Os and Ir, Chihuahua City has the lowest concentrations of Ru and Pt, and Union County has the lowest concentration of Pd. As such, relating the IC irons by simple crystal-liquid fractionation processes is problematic.

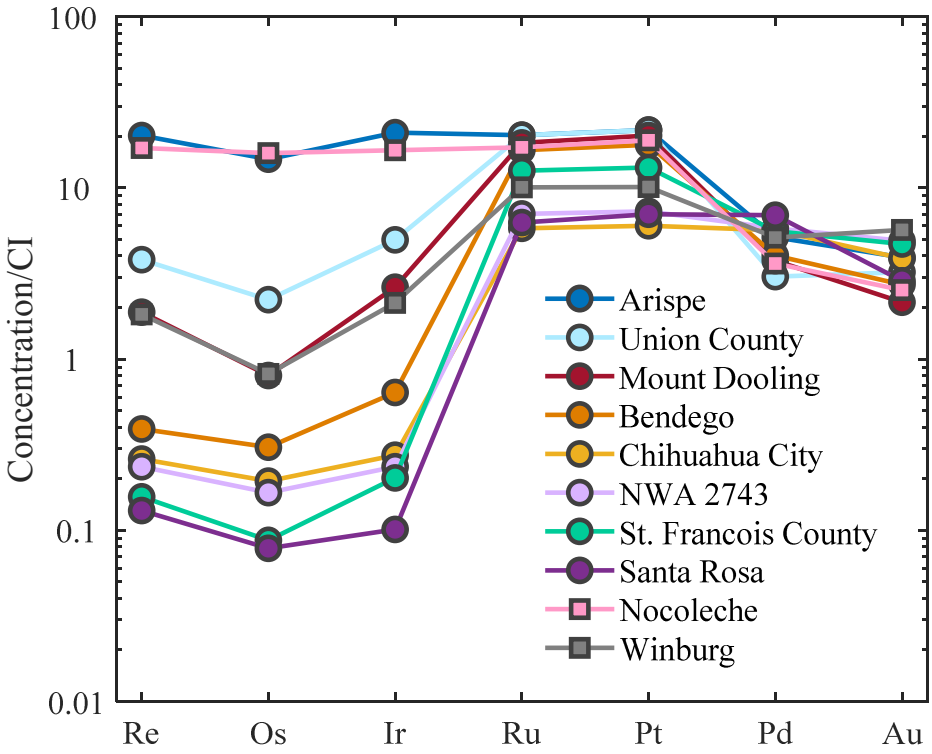

Figure 3.4 Bulk CI chondrite normalized abundance plot of HSE abundances. Data for all HSE except Au were obtained by isotope dilution for bulk samples of the IC irons. The Au data were obtained by laser ablation ICP-MS. Bulk composition data were normalized to Re, Os, Ir, Ru, Pt and Pd concentrations for the CI chondrite Orgueil reported by Horan et al. (2003) and Au data were normalized to average Au concentrations of CI chondrites reported by Fischer-Gödde et al. (2010).

3.5. Discussion

3.5.1. Parent Body Genetics

Molybdenum and W isotopes are useful for distinguishing between NC and CC type meteorites because they are created by a combination of *p-, r-,* and *s*-process nucleosynthesis. The distinctive nucleosynthetic signatures are useful for assessing genetic relations within and among iron meteorite groups.

The $^{97}Mo/^{96}Mo$ ratio is minimally affected by CRE (Worsham et al., 2017) and is measured with the highest level of precision in this study. As such, we use $\mu^{97}Mo$ values for genetic comparisons. Nocoleche and Winburg have $\mu^{97}Mo$ values that are much lower than Arispe, Bendego and Chihuahua City. Most IC irons have $\mu^{97}Mo$ values that are similar to those of other magmatic NC type irons (Fig. 3.5). Nocoleche has a $\mu^{97}Mo$ value that is within uncertainty of the terrestrial Mo standard and overlaps with one ungrouped iron, Gebil Kamil. The resolvedly different $\mu^{94,95,97}Mo$ values for Nocoleche and Winburg indicate nucleosynthetic Mo isotope heterogeneity among members of the purported IC group. Additionally, the higher $\mu^{182}W$ values for Nocoleche and Winburg provide permissive evidence that they may not be IC irons. Thus, it is likely Nocoleche and Winburg were derived from a distinct parent body from that of Arispe, Bendego and Chihuahua City and will not be considered further as a members of the IC group.

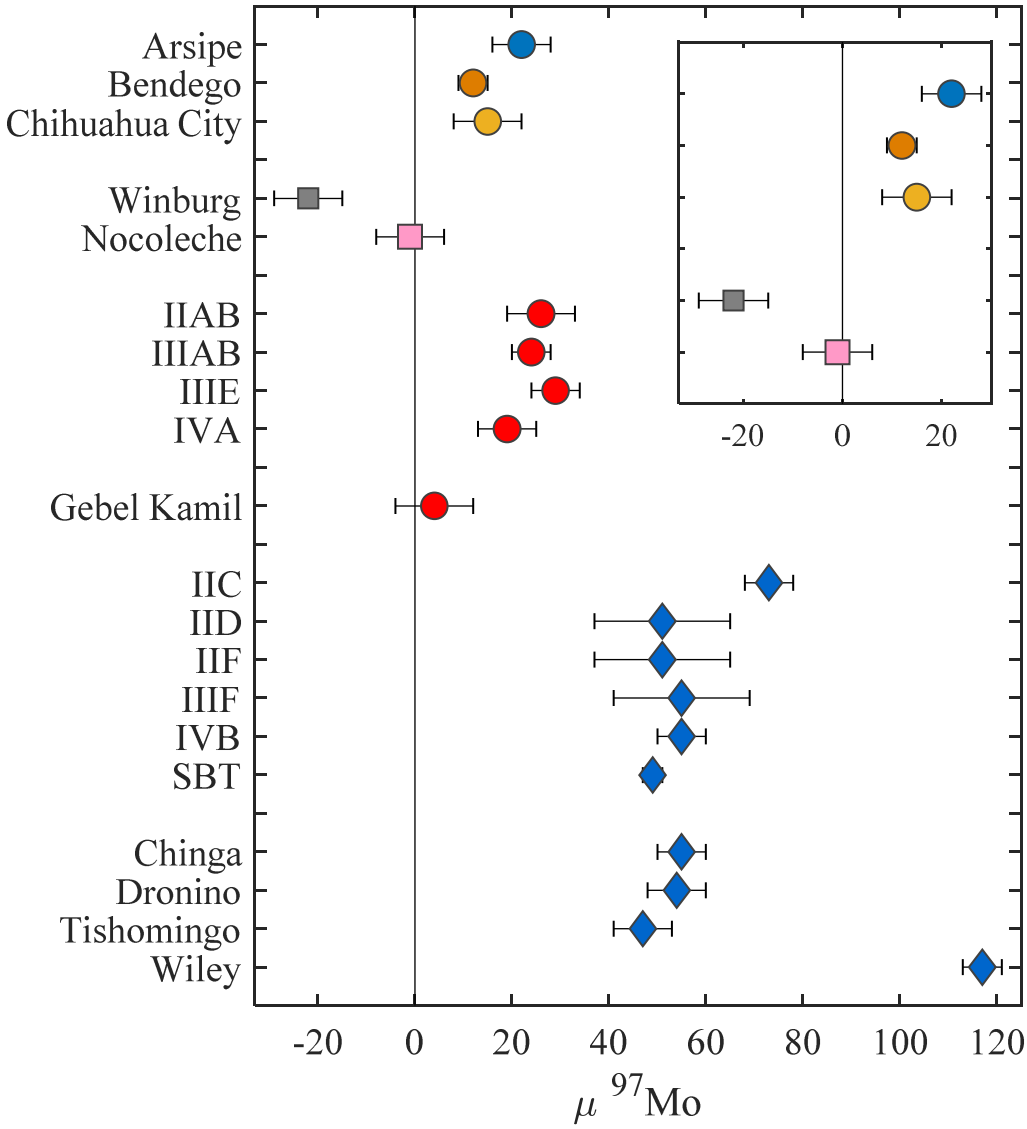

Figure 3.5 Cosmic ray exposure uncorrected μ^{97}Mo variation for the IC group and Nocoleche. For comparison, μ^{97}Mo values of magmatic iron meteorite groups and ungrouped irons are shown (Bermingham et al., 2018, Worsham et al., 2019 and Hilton et al., 2019). Red and blue symbols are NC and CC types, respectively. Error bars for the IC irons and Nocoleche reflect the 2SD of repeated analysis of the terrestrial standard during the respective analytical campaign.

The NC and CC types are characterized by *s*-process deficits, while the CC type groups possess an additional *r*-process excess. Both groups fall along two apparent *s*-process mixing lines on a plot of μ^{94}Mo versus μ^{95}Mo (Budde et al., 2016; Poole et al.,

2017; Worsham et al., 2017) (Fig. 3.6). The average μ^{94}Mo, μ^{95}Mo and μ^{97}Mo values for Arispe, Bendego and Chihuahua City are +81 ± 6, +23 ± 3 and +14 ± 4, respectively. These values are consistent with the averages reported by Poole et al. (2017) and Worsham et al. (2019), studies in which more than one IC was measured. Nocoleche and Winburg fall slightly below the NC *s*-process mixing line, likely because they have not yet been corrected for CRE. The average Mo isotopic compositions of the IC group is identical, within uncertainties of those determined for the NC type IVA iron meteorite group (Bermingham et al., 2018; Worsham et al., 2019). Except for μ^{97}Mo, Nocoleche and Winburg have Mo isotopic compositions that are identical, within uncertainties of those determined for the NC type IIAB iron meteorite group (Bermingham et al., 2018; Worsham et al., 2019).

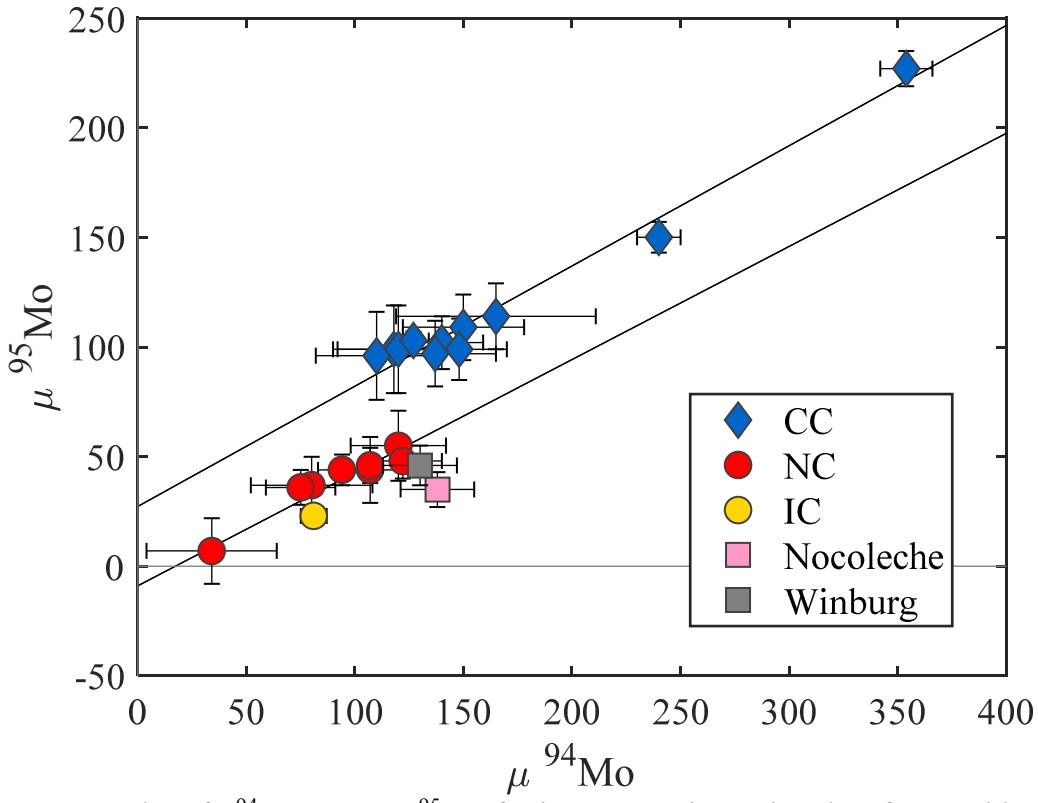

Figure 3.6 Plot of μ^{94}Mo versus μ^{95}Mo for iron meteorites using data from Table 3.1 and group averages reported by Bermingham et al. (2018), Worsham et al. (2019), Hilton et al. (2019) and Tornabene et al. (2020). NC type meteorites include group averages of IIAB, IIIAB, IIIE, IVA and two ungrouped irons, Nocoleche and Gebel Kamil. CC type meteorites include group averages of IID, IIF, IIIF, IVB, SBT, IIC and four ungrouped irons Wiley, Chinga, Dronino, and Tishomingo. The black lines are linear regressions calculated using *ISOPLOT*.

3.5.2. Radiogenic W isotope variations

A model age of metal segregation (ΔT_{CAI}) in iron meteorites can be calculated using Eq. 1.1. In order to calculate accurate and precise ages of core formation, cosmic ray-induced shifts to the μ^{182}W value of a given meteorite must be known. Thus, the ages of core formation given in Table 3.2 should be taken with caution. Nonetheless, the spread of μ^{182}W values between Arispe, Bendego and Chihuahua City is hard to reconcile by formation from a single parent body.

3.5.2. Re-Os isotopic system

Most IC irons plot on or near a primordial isochron indicating that the IC suite was generally a closed system and their HSE abundances reflect those at the time of crystallization. Chihuahua City and Mount Dooling do not plot within uncertainty of a primordial isochron but are only offset by -3.1 and +2.1%, respectively. As such, they likely have absolute HSE abundances that reflect minor loss or gain of Re and Os. These minor offsets are unlikely to affect fractional crystallization modeling discussed below.

3.5.3. Crystallization models

The essentially uniform Mo and ^{183}W isotopic compositions for the *bona fide* IC irons analyzed in this study are suggestive of their formation on the same parent body. The HSE patterns of the IC group are broadly consistent with fractional crystallization in that concentrations of Re, Os, Ir, Ru, and Pt, normally characterized by solid metal-liquid metal D values >1 (where D values are solid/liquid concentration ratios), decrease in metal as crystallization proceeds, while Pd (normally characterized by solid metal-liquid metal D values <1), increases. In this study, appropriate solid metal-liquid metal D values for the HSE were calculated using the parameterization method developed by Chabot et al. (2017) and discussed in detail in Chapter 1 and supplementary materials. The parameterization depends on the mole fractions of S, P and C. The initial abundances of these light elements are used as the main input variables to calculate D values that can best account for the range of HSE concentrations of the IC group.

As has been done for other iron meteorite groups (Wasson, 1999; Chabot, 2004; Goldstein et al., 2009), an initial bulk S content is estimated from the Ga and Ge versus Au

trends. Gallium, Ge and Au partition are sensitive to bulk S concentrations and produce distinct non-linear trends. Thus, these elements serve as good proxies to constrain initial S. Figure 3.7 shows data for the IC irons as well as results for simple fractional crystallization trends for estimates of initial S contents. Due to the significant scatter on the two diagrams, there is no trend that best fits all IC data. However, the modeled results best fit the IC data with relatively higher initial S contents between 13 wt% and 23 wt% (Fig. 3.7).

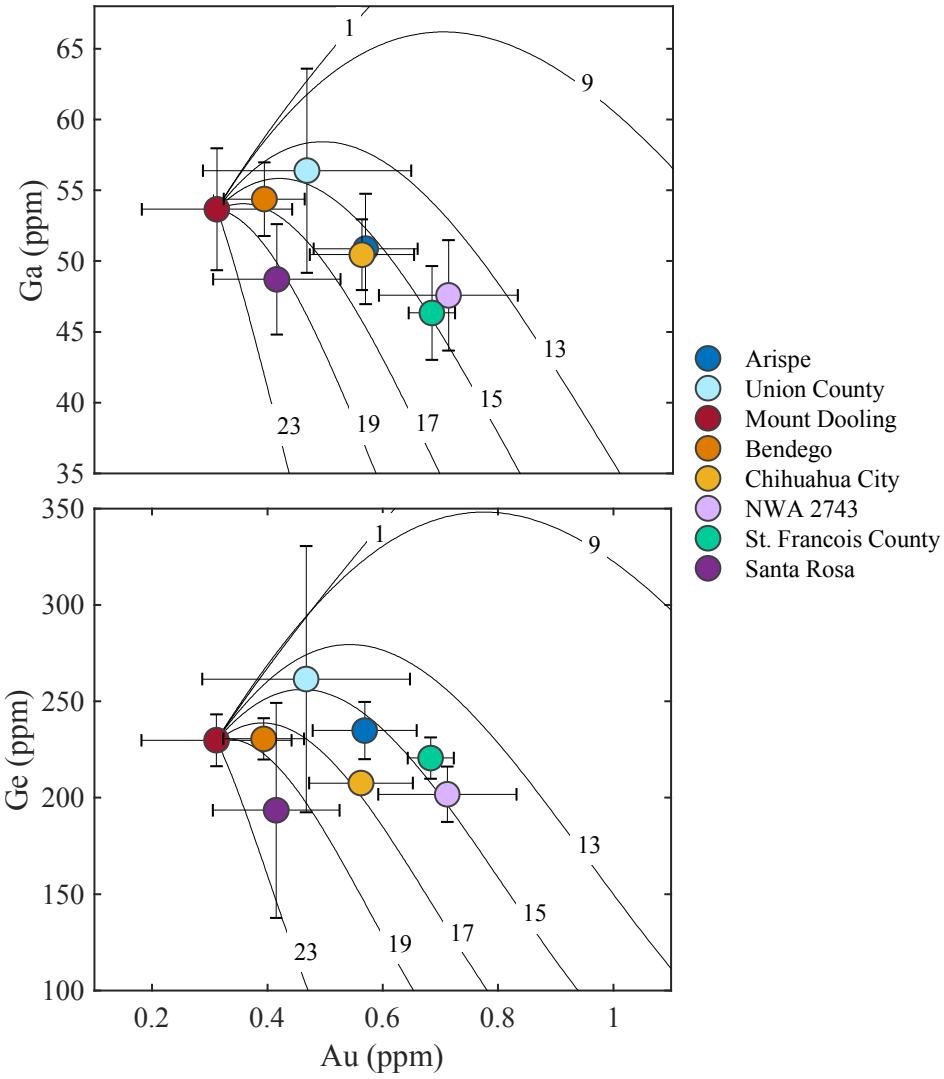

Figure 3.7 Plots of Au (ppb) versus Ge and Ga (ppb). Solid lines represent fractional crystallization trends as determined by models between 5 wt% and 23 wt% initial S contents.

We constrain initial P and C content by dividing the average P and C composition of the least evolved IC iron (Arispe) by the constant D_o values (where D_o is the solid metal-liquid metal D value in the light-element-free Fe-Ni system) for P (0.1) and C (0.4) (Chabot et al., 2017). This method suggests an initial P and C content of approximately 0.1 wt% and 0.01 wt%, respectively. Due to the large range in estimated initial S contents given in Fig. 3.5, we consider both relatively low and high initial S contents of 1 and 19 wt.% S, respectively.

For the modeling conducted here, Re and Os are considered first because they are the best measured HSE and we assume their initial concentration ratio were within the chondritic range. Arispe is assumed to represent the earliest formed solid to crystallize as it has the highest Re and Os concentrations, and is the least fractionated sample of the IC group. Model solid and liquid evolution tracks of Re concentration versus Re/Os with data for the IC irons are shown in Figure 3.8a-b. Figure 3.8a and 3.8b model evolution tracks of solid and liquid assuming initial S contents of 1 and 19 wt.%, henceforth referred to as models A and B, respectively. In both models, the higher-Re and Os irons (Arispe, Union County and Mount Dooling) all fall between the solid and liquid tracks. Problems with models A and B are apparent as Bendego, Chihuahua City, NWA 2743, St. Francois County and Santa Rosa do not plot between the solid and liquid tracks. These more evolved, lower-Re and Os irons plot to the left of the liquid tracks (Fig. 3.8a-b) and cannot be accounted for by simple crystal-liquid fractionation models, which predict concentrations of Re and Os that are much higher than observed for the low abundance IC irons. The large differences between the high and low Re and Os abundance irons may be understood if the low abundance irons (Bendego, Chihuahua City, NWA 2743, St. Francois

County and Santa Rosa) were formed as variable mixtures of equilibrium solid and melt. This scenario is best understood if they represent mixing between early formed solids (high Re and Os) and evolved liquids (low Re and Os).

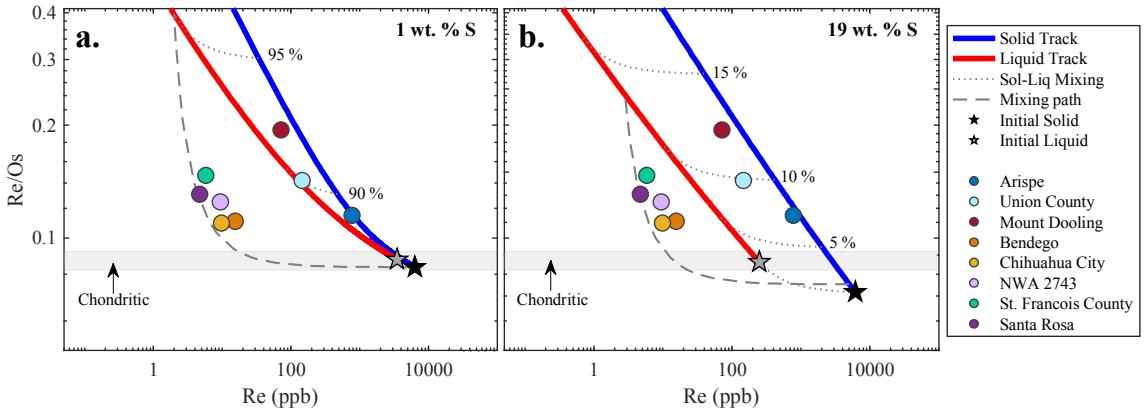

Figure 3.8a-b Simple fractional crystallization and equilibrium mixing models for Re (ppb) versus Re/Os. The grey area is the range of chondrites (Walker et al. 2002). The colored symbols are the data for the IC irons. The black star represents the composition of the first solid to form. The grey star represents the starting liquid composition. The blue line represents the solid track and the red line represents the liquid track. The dotted grey lines show mixing curves connecting the equilibrium solid and liquid tracks at 5% increments. The grey dashed lines show potential mixing curves of an evolved melt with an equilibrium solid at approximately 1% fractional crystallization. **(a)** Fractional crystallization model defined by 1 wt.% initial S. **(b)** Fractional crystallization model defined by 19 wt.% initial S. Both **(a)** and **(b)** are calculated for identical initial P and C contents discussed in the text.

In a crystallizing core, an infinite number of different mixing processes are possible. For simplicity, we model the low abundance group as being mixtures of an early formed solid at ~1% fractional crystallization with an evolved liquid at least ~95% (Fig. 3.8a) and ~13% (Fig. 3.8b). All IC irons can be accounted for in both models. Cook et al. (2003) suggested that this type of mixing could have been a result of an injection of liquids into a solid core. This mechanism could have been a result of a disturbance to the IC core, possibly from an impact, consistent with the conclusions of Scott (1977) which suggested a collision soon after IC core crystallization that fragmented and dispersed some IC irons.

Next, we model Pt-Os systematics using the same initial parameters as those for Re-Os. Model solid and liquid evolution tracks of Pt concentration versus Pt/Os with IC data are shown in Figure 3.9a-b and provide very different results from Re-Os systematics.

If the IC irons were formed by the above mixing mechanism proposed for Re-Os, the iron positions relative to the solid and liquid tracks would be consistent for all element pairs. For example, Bendego, Chihuahua City, NWA 2743, St. Francois County and Santa Rosa would all be expected to plot to the left of the liquid track on Pt versus Pt/Os plots. This is not observed as all IC samples plot between the solid and liquid tracks (Fig 3.9a-b). The ability to successfully model Pt/Os and not Re/Os by simple fractional crystallization could be a result of processes other than fractional crystallization that caused significant scatter in Re abundances, misclassification of some irons, and/or inaccurate D values used in the models presented here.

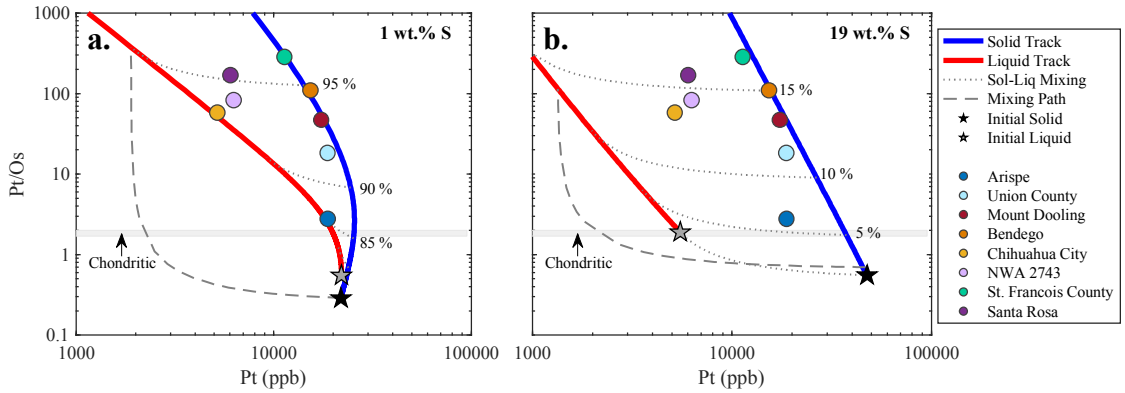

Figure 3.9a-b Simple fractional crystallization and equilibrium mixing models for Pt (ppb) versus Pt/Os. The grey area is the range of chondrites (Walker et al. 2002). The colored symbols are the data for the IC irons. The black star represents the composition of the first solid to form. The grey star represents the starting liquid composition. The blue line represents the solid track and the red line represents the liquid track. The dotted grey lines show mixing curves connecting the equilibrium solid and liquid tracks at 5% increments. The grey dashed lines show potential mixing curves of an evolved melt with an equilibrium solid at approximately 1% fractional crystallization. **(a)** Fractional crystallization model defined by 1 wt.% initial S. **(b)** Fractional crystallization model defined by 19 wt.% initial S. Both **(a)** and **(b)** are calculated for identical initial P and C contents discussed in the text. Of note, both models can account for the observed concentrations of the IC irons however, the starting liquid composition of the model define by 1 wt.% initial S falls significantly below the range of chondrites.

While the IC irons can be modeled with both low and high initial S concentrations, our preferred model utilizes 19 wt.% S (model B). This is because with lower initial S

estimates, the starting liquid composition of the IC parental melt falls substantially below the normal range of bulk chondrites (Fig. 3.9a). This defies the assumption that metal cores segregated from a melt with chondritic relative abundances of HSE. Additionally, the limited spread between the solid and liquid tracks for Pt-Os model A requires Arispe to fall along the liquid track, representing an equilibrium liquid composition. This is inconsistent with Re-Os model A where Arispe is modeled as having an equilibrium solid composition. Model B does not generate consistent relative positions from the solid and liquid tracks, however, model B can successfully account for all IC irons as crystallizing from a chondritic parental melt. Finally, previous studies have noted a correlation between $\mu^{182}W$ values of magmatic iron meteorite groups and inferred S contents for their respective cores (Kleine and Walker, 2017; Hilton et al., 2019). If true, the $\mu^{182}W$ value for the IC group would suggest a relatively S-rich body.

We conclude that the IC group was likely formed by processes other than simple crystal-liquid fractional crystallization. There is suggestive evidence that the IC core experienced late-stage parent body modification, occurring within the first 100 Myr of solar system history. If a late-stage impactor was volatile rich, Re/Os could be modified by aqueous alteration (Worsham et al., 2016). This could potentially explain the inconsistencies between Re-Os modeling and modeling of the other HSE.

The initial melt concentrations of HSE calculated from the preferred Model B for the IC parent body core are given in Table 3.5, along with estimated initial HSE concentrations for the magmatic group IVB, IVA, IIC, and South Byron Trio (SBT) irons for comparison (Walker et al., 2008; McCoy et al., 2011; Tornabene et al., 2020; Hilton et al., 2019). Results are shown in Figure 3.10 along with the patterns representative of

average carbonaceous and enstatite chondrites (Horan et al., 2003). If the average HSE composition of enstatite chondrites is assumed to be the starting concentration of the IC parent body (both NC type), then the IC group is approximately 4 times higher than the enstatite chondrite average. Assuming ~99% of HSE were extracted into the core, the IC core would have comprised ~25% of the mass of the body. The estimated HSE pattern of the IC group is comparatively lower than those of the CC type SBT and IVB groups. Lower concentrations of HSE are likely a result of a lower proportion of oxidized iron remaining in the mantle of the parent body. This is consistent with the IC parent body forming in a relatively more reducing environment than that of the IVB and SBT parent bodies. The NC nebular reservoir is commonly envisioned as having been a more reducing environment compared to the CC reservoir.

Table 3.5 Calculated initial concentrations of HSE (in ppb) for the parameters discussed in the text.

	Re	Os	Ir	Ru	Pt	Pd	Au
IC	250	2900	2700	4200	5500	3500	700
IIC[a]	280	3350	3050	4340	6070	5300	1350
IVB[b]	2800	37000	27000	27400	29500	8600	150
IVA[c]	295	3250	2700	3900	5900	4500	1320
SBT[d]	770	9400	8500	13000	16000	8400	2200[e]

[a] Data from Tornabene et al., (2020); [b] Data from Walker et al. (2008); [c] Data from McCoy et al. (2011); [d] Data from Hilton et al. (2019), SBT – South Byron Trio; [e] Data from McCoy et al. (2019).

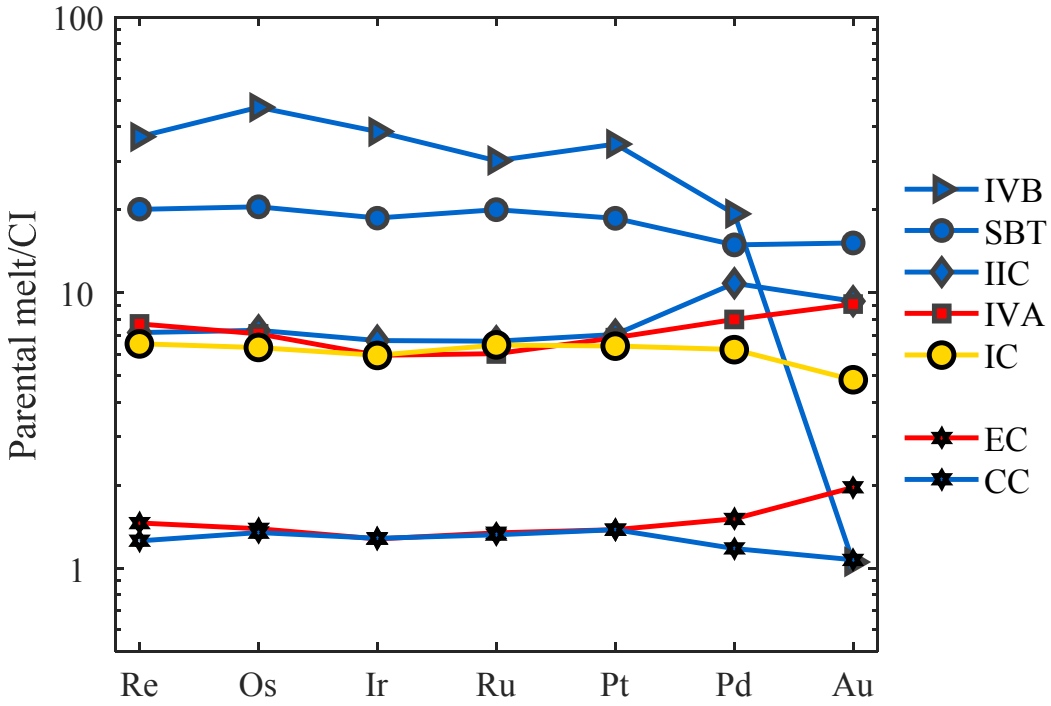

Figure 3.10 Plot of calculated parental melt HSE concentrations, normalized to Re, Os, Ir, Ru, Pt and Pd concentrations for the CI chondrite Orgueil reported by Horan et al. (2003) and Au data were normalized to average Au concentrations of CI chondrites reported by Fischer-Gödde et al. (2010). Parameter concentrations are plotted from Table 3.6. For comparison, the initial parental melt concentrations estimated by Walker et al., 2008 (IVB), McCoy et al., 2011 (IVA), Hilton et al., 2019 (SBT) and Tornabene et al., (2020) are shown.

3.6. Conclusions

1) Cosmic ray exposure uncorrected Mo and W isotopic compositions for Arispe, Bendego and Chihuahua City are generally consistent with formation from the same parent body within the NC nebular reservoir. Nocoleche and Winburg have Mo isotopic compositions that suggest it is distinct from the other IC irons analyzed here, but is also of the NC type.

2) Siderophile element abundances of IC iron meteorites are generally similar, which is inconsistent with their wide range of diverse mineral textures. The distribution of HSE in the IC group, however, cannot be accounted for by simple fractional

crystallization. Our results are consistent with the interpretation that the IC core experienced late-stage parent body modification. Such modification could not have been extensive as to disturb the Re-Os isotopic systematics, which indicate the IC suite was generally a closed system. A chondritic parental melt composition can be estimated for the IC core, assuming a metallic melt containing 19 wt.% initial S, 0.1 wt% initial P and 0.01 wt% initial C concentrations.

Chapter 4: Summary of Research Conclusions

The chemical and isotopic characteristics of diverse iron meteorite groups provide insights into the planetary and nebular heterogeneity present in the early solar system. The IC and IIC iron meteorites allow for the examination of accretionary processes, crystal-liquid fractionation, and genetic diversity of understudied and "rare" irons. Their isotopic differences indicate they formed in distinct regions and/or at different times in the protoplanetary disk.

Highly siderophile element abundances of the IC and IIC irons suggest that different crystallization processes took place during the accretion and solidification of these planetary bodies. The IIC iron meteorites are consistent with simple fractional crystallization of a core that began crystallization with a moderate initial S content of 8 wt.%. Modelling suggests that bulk compositions of the IIC irons can be accounted for as equilibrium solids, liquids or mixtures of both. The corresponding IIC parent melt provides evidence for a relatively oxidizing nebular environment, but one that was less oxidizing than other CC type bodies. Nucleosynthetic Mo and W isotope evidence indicates that subsequent nebular processing to the IIC parent body likely generated their anomalous isotopic compositions, although the cause remains elusive.

Modeling results suggest a different crystallization history for the IC irons and that processes beyond simple crystal-liquid fractionation took place. The large differences in the siderophile element abundances of the IC group cannot be accounted for by simple fractional crystallization. Instead, they may represent formation from an initial metallic melt with ~19 wt.% S, as variable mixtures of fractionally crystallized solid and trapped liquid that resulted from a disturbance to the parent body. This type of evolution is not

commonly envisioned for the other major magmatic iron groups. The IC core likely experience late-stage parent body modification, which could explain its more complex history including the large differences in calculated cooling rates reported by prior studies. The estimated IC parental melt composition indicates formation under only slightly more reducing conditions relative to the IIC parent body.

The Mo isotopic compositions of the irons analyzed indicate the IC and IIC iron meteorites formed in genetically distinct nebular domains. Nocoleche and Winburg have Mo isotopic compositions that are distinct from those of the IC irons. The IC irons and Nocoleche are of the NC type and are characterized by *s*-process deficits. Nocoleche and Winburg are characterized by enrichments of μ^{94}Mo relative to μ^{95}Mo, compared to the IC group, indicating an additional enrichment in *s*- and *r*-process Mo. The IIC irons and Wiley exhibit the largest nucleosynthetic ^{94,95,97}Mo isotope anomalies of any iron meteorite group analyzed to date. The IIC group and Wiley plot along an apparent *s*-process mixing line with the CC type irons, suggesting they may by of the CC type.

Expanding research to additional ungrouped irons may widen our knowledge of the current structure of the early solar system. To date, the IIC irons and Wiley exhibit the largest known nucleosynthetic isotope anomalies in iron meteorites. Their extreme compositions raise the question of whether there are additional nebular domains beyond what we have identified as NC and CC.

Supplementary Materials

Chapter 2

Data Comparison

Comparisons between literature data and this study are provided in Table S1 for Mo. Literature data are generally in good agreement with this study.

Table S2.1 Comparison between literature Mo isotopic data and the data from this study. Data from the literature were monitored for cosmic ray exposure.

	Reference	n	μ^{94}Mo	2σ	μ^{95}Mo	2σ	μ^{97}Mo	2σ
IIC Average								
	Kruijer et al. (2017)[a]	2	+227	21	+115	14	+84	14
	Poole et al. (2017)	3	+240	16	+161	9	+82	5
	Worsham et al. (2019)	4	+225	10	+156	7	+83	7
	This study	3	+248	6	+156	6	+73	10
Wiley Average								
	Kruijer et al. (2017)	8	+339	13	+219	11	+119	11
	Worsham et al. (2019)	3	+342	7	+223	8	+112	7
	This study	2	+356	11	+230	5	+118	2

[a] IIC data were not reported as an average. These values were recalculated from the published data.

Fractional Crystallization Modeling

In this study, appropriate solid metal-liquid metal D values (concentration ratios) for the HSE were calculated using the parameterization method developed by Jones and Malvin (1990) and advanced by Chabot et al. (2017):

$$\text{Eq. S1: } \frac{1}{D} = \frac{(\text{Fe Domains})^{(\beta_{SP})}}{D_o}$$

where D_o is the solid metal-liquid metal D value in the light-element-free Fe-Ni system experimentally determined by Chabot et al. (2017). Iron domains are calculated by:

$$\text{Eq. S2: Fe Domains} = \frac{(1-2X_S-4X_P)}{(1-X_S-3X_P)}$$

where X_S is the mole fraction of S in the metallic liquid, X_P is the mole fraction of P in the metallic liquid, and β_{SP} is a constant specific to the element being parameterized calculated by:

$$\text{Eq. S3: } \beta_{SP} = \left[\frac{2X_S}{(2X_S+4X_P)}\right]\beta_S + \left[\frac{4X_P}{(2X_S+4X_P)}\right]\beta_P$$

where β_S and β_P are constants specific to the elements being parameterized experimentally calculated by Chabot et al. (2017). A constant D value for S of 0.001 is used and the D value for P is calculated using Eq. 1.

Liquid HSE concentration (C_L) is calculated by:

$$\text{Eq. S4: } C_{Ln} = \frac{C_{L\,(n-1)}}{F_{n-1}+1-F_{n-1}D_{n-1}}$$

where F_n is the fraction of liquid and D_n is the partition coefficient of a given element calculated at that fraction of crystallization. Solid HSE concentration (C_S) is calculated by:

$$\text{Eq. S5: } C_S = C_L D$$

Equations 1-5 are re-calculated for each increment of crystallization.

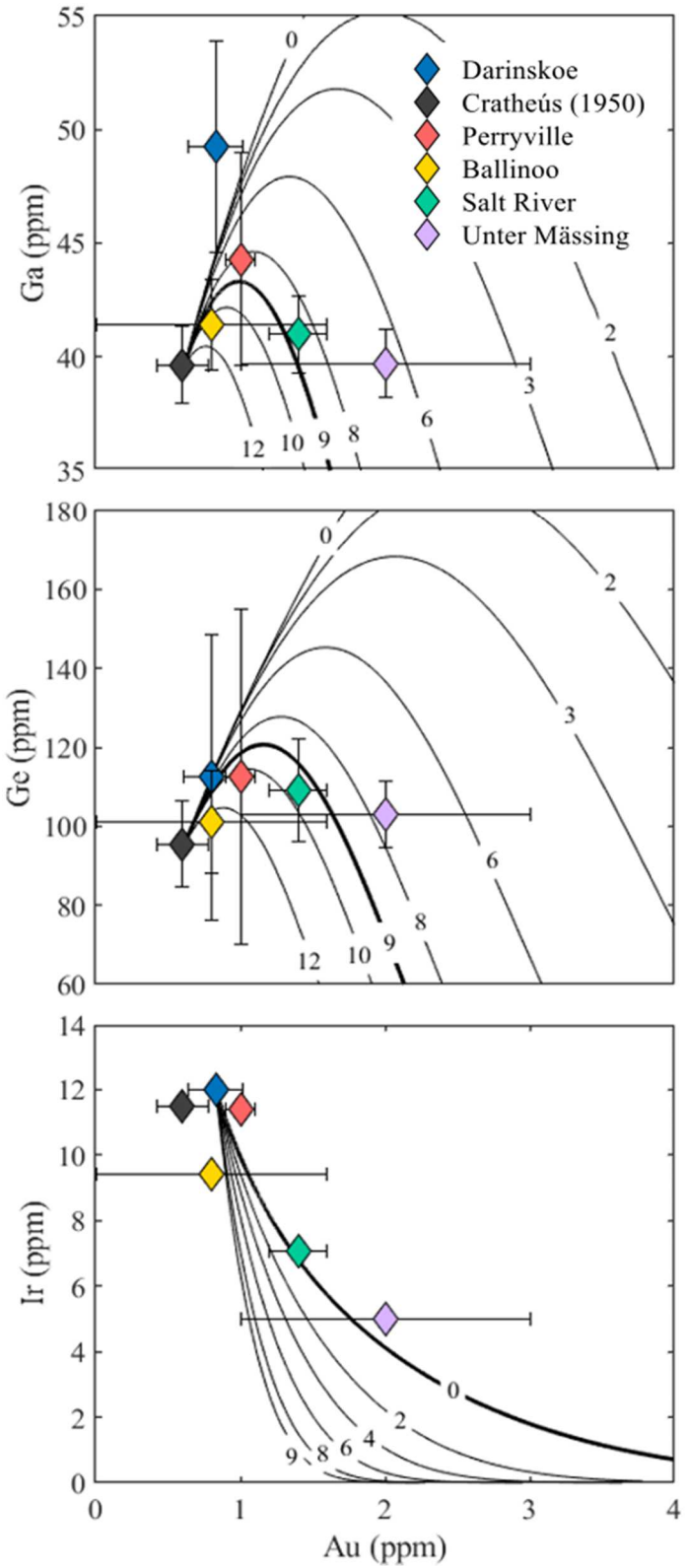

Figure S2.1 Plots of Au (ppm) versus Ga, Ge, and Ir (ppm). Solid lines represent the best fit estimates for S. Gold data for Kumerina determined by laser ablation were below detections limits.

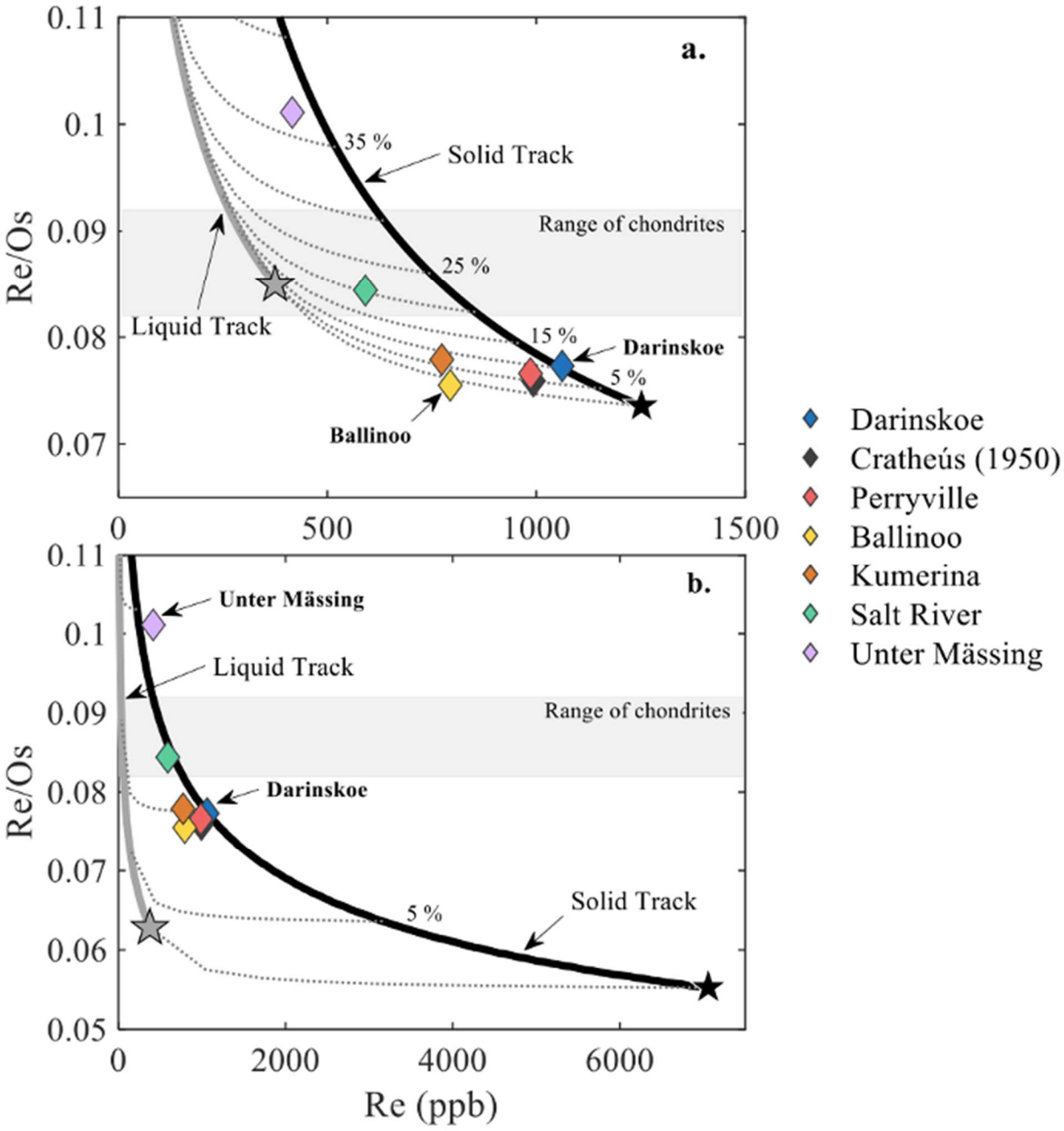

Figure S2.2a-b. Fractional crystallization model for Re (ppb) versus Re/Os calculated for initial set of parameters defined by 4 wt.% S and 3 wt.% P (Fig. S2a) and 16 wt.% S and 1 wt.% P (Fig. S2b) concentrations. The grey area is the range of chondrites (Walker et al., 2002). The colored diamonds are the data for the IIC irons. The black line represents the solid track and the grey line represents the liquid track. The dashed grey lines show mixing curves connecting the equilibrium solid and liquid tracks at 5% increments. The black and grey stars represent the first solid and liquid composition to form, respectively. Neither model can account for all IIC irons (Ballinoo in model A and Unter Mässing in model B).

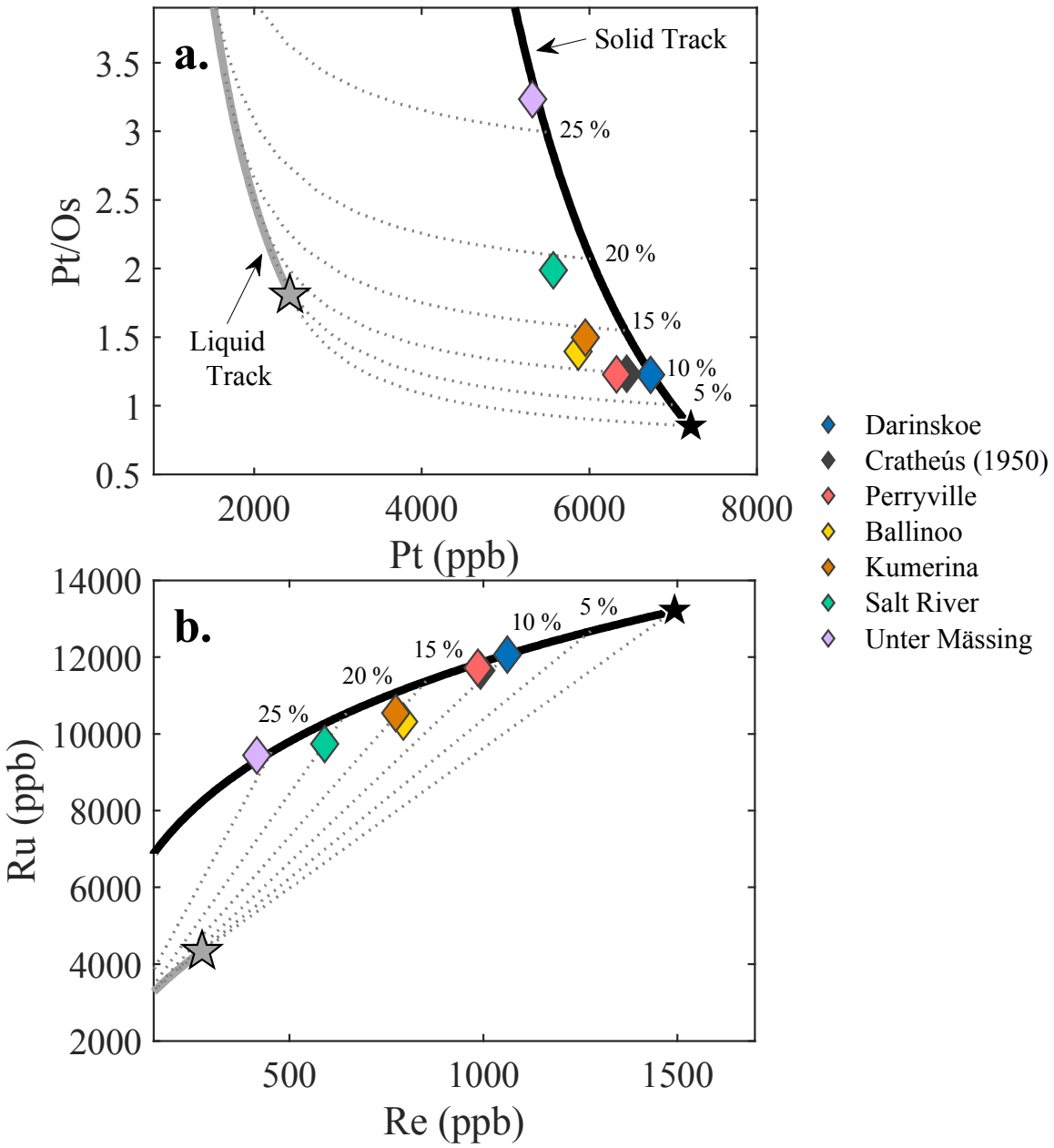

Figure S2.3a-b. (a) Fractional crystallization model for Pt (ppb) versus Pt/Os calculated for initial S and P concentrations of 8 and 2 wt.%, respectively (Model B in the main text). **(b)** Fractional crystallization model for Re (ppb) versus Ru (ppb) calculated for initial S and P concentrations of 8 and 2 wt.%, respectively (Model B in the main text). In both figures, the black line represents the solid track and the grey line represents the liquid track. The dashed grey lines represent mixing curves connecting the equilibrium solid and liquid tracks at 5% increments. colored diamonds are the data for the IIC irons. The black and grey stars represent the first solid and liquid composition to form, respectively. These fractional crystallization models are in good agreement with the Re (ppb) versus Re/Os model B in the main text. For example, Unter Mässing plots on the solid track in both models, representing a solid crystallization at approximately 26% fractional crystallization.

Tungsten-182 Correction

The IIC group and Wiley average $\mu^{182}W$ values were corrected for nucleosynthetic W isotope variations using the method reported by Kruijer et al. (2014). This was done by using the mean $\mu^{183}W$ value for the IIC group and Wiley and the $^{182/184}W$ *vs.* $^{183/184}W$ (186/184 normalized) isotopic composition obtained for CAIs, which gives a slope value of $+1.41 \pm 0.06$.

Thermal Accretion Model

This study uses the thermal accretion model described by Kruijer et al. (2017) and Hilton et al. (2019). In brief, the model uses the IIC group and Wiley's calculated differentiation ages and uncertainties to estimate parent body accretion ages. This model calculates temperature at a depth within a solid sphere that gains heat by ^{26}Al decay. Within the model, temperature is tracked halfway to the center of the body from the surface until it reaches 1600 K, at which point differentiation is assumed to occur instantly. The parent body concentration of Al is assumed to be between 0.86-1.68 wt.%, determined from the range observed in carbonaceous chondrites (Lodders and Fegley, 1998).

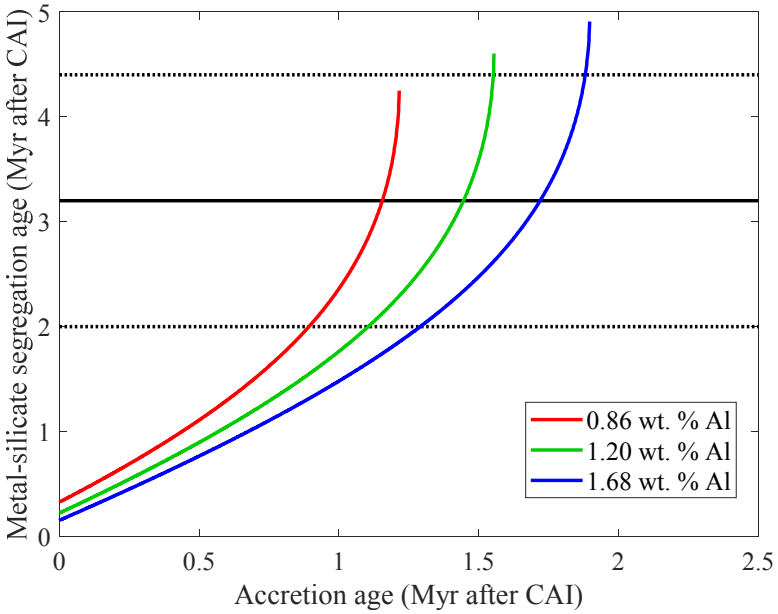

Figure S2.4 Thermal model results for Al concentrations of 0.86, 1.20 and 1.68 wt.%. The differentiation age for the IIC group of 3.2 ± 0.7 Myr after CAI formation (black solid line) corresponds to an accretion age of 1.4 ± 0.5 Myr after CAI formation.

Supplementary Figures for Chapter 1

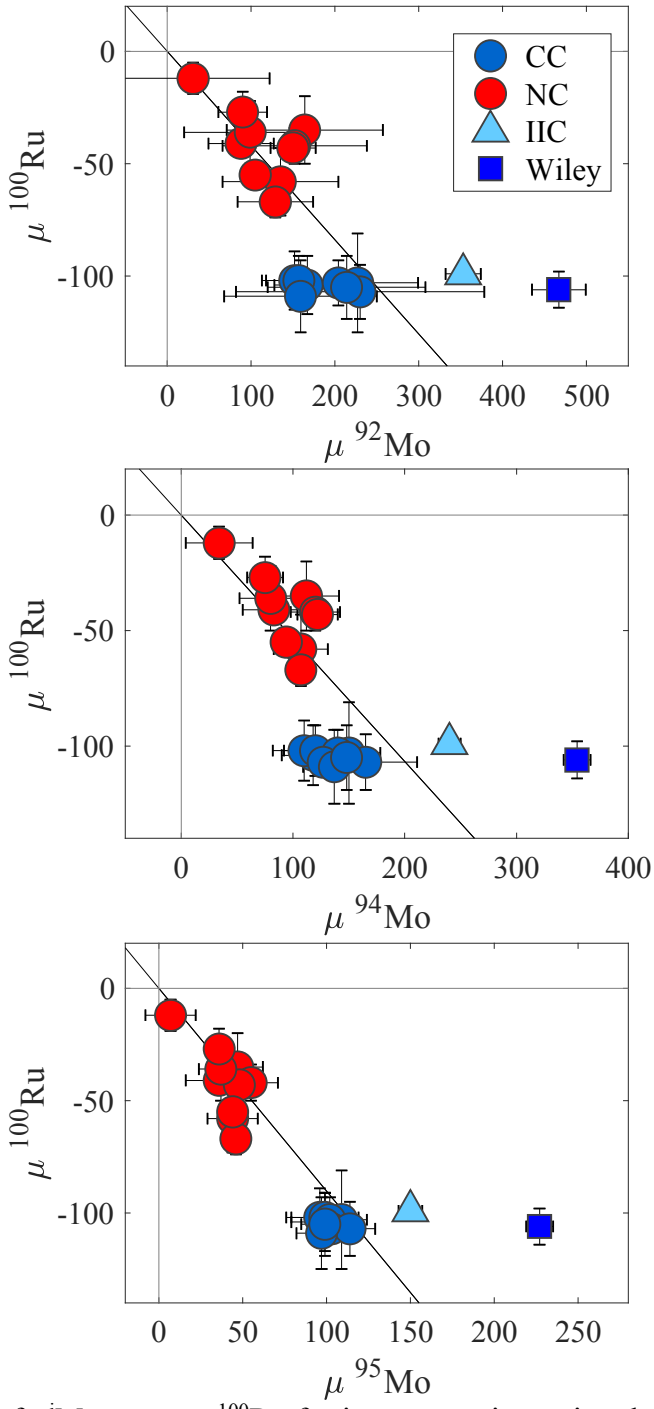

Figure S2.5 Plots of μ^{i}Mo versus μ^{100}Ru for iron meteorites using data from Table 4 and group averages reported by Bermingham et al. (2018), Worsham et al., (2019) and Hilton et al. (2019). NC type meteorites include group averages of IC, IIAB, IIIAB, IIIE, IVA and one ungrouped iron, Gebel Kamil. CC type meteorites include group averages of IID, IIF, IIIF, IVB, SBT, IIC and four ungrouped irons Wiley, Chinga, Dronino, and Tishomingo. The black lines are linear regressions calculated using *ISOPLOT*.

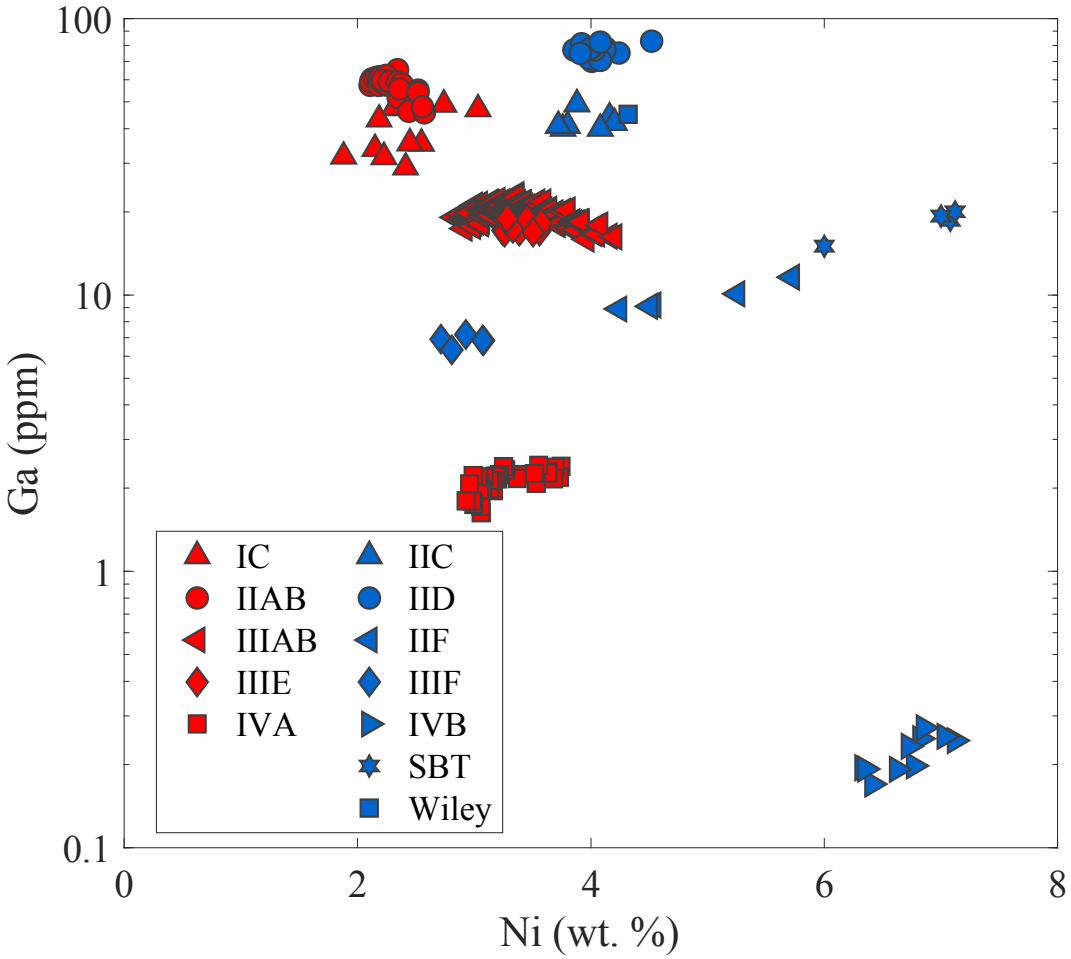

Figure S2.6 Plot of Ni (wt.%) versus Ga (ppm) using data from this study, Walker et al. (2008), McCoy et al. (2011), Hilton et al. (2019), and numerous studies from the UCLA Wasson group, e.g., Scott et al. (1973), Scott and Wasson (1976), Kracher et al. (1980), and Wasson (1999). Blue symbols are the CC bodies and red symbols are the NC bodies.

Data Comparison

Table S3.1 Comparison between literature Mo isotopic data and the data from this study. Data from the literature were monitored for cosmic ray exposure, indicating any cosmogenic effects were minimal.

	Reference	n	$\mu^{94}Mo$	2σ	$\mu^{95}Mo$	2σ	$\mu^{97}Mo$	2σ
Arispe								
	Burkhardt et al. (2011)	4	74	25	17	29	10	12
	Poole et al. (2017) [a]	4	89	18	29	13	20	8
	Worsham et al. (2019)	5	75	14	21	10	14	7
	This study	1	78	10	23	6	22	6
Bendego								
	Poole et al. (2017)	2	87	20	26	7	16	11
	Bermingham et al. (2018)	2	112	29	47	15	24	7
	Worsham et al. (2019)	5	83	13	26	6	23	11
	This study	3	85	3	22	6	12	3
Chihuahua City								
	Worsham et al. (2019)	8	86	8	34	7	20	8
	This study	1	72	17	27	8	15	7

[a] Arispe data were not reported as an average. These values were recalculated from the published data.

References

Allègre, C. J., & Luck, J. M. (1980). Osmium isotopes as petrogenetic and geological tracers. *Earth and Planetary Science Letters*, ***48***(1), 148-154.

Archer, G. J., Mundl, A., Walker, R. J., Worsham, E. A., & Bermingham, K. R. (2017). High-precision analysis of $^{182}W/^{184}W$ and $^{183}W/^{184}W$ by negative thermal ionization mass spectrometry: Per-integration oxide corrections using measured $^{18}O/^{16}O$. *International Journal of Mass Spectrometry*, ***414***, 80-86.

Arlandini, C., Käppeler, F., Wisshak, K., Gallino, R., Lugaro, M., Busso, M., & Straniero, O. (1999). Neutron capture in low-mass asymptotic giant branch stars: cross sections and abundance signatures. *The Astrophysical Journal*, ***525***(2), 886.

Bermingham, K. R., Walker, R. J., & Worsham, E. A. (2016). Refinement of high precision Ru isotope analysis using negative thermal ionization mass spectrometry. *International Journal of Mass Spectrometry*, ***403***, 15-26.

Bermingham, K. R., Worsham, E. A., & Walker, R. J. (2018). New insights into Mo and Ru isotope variation in the nebula and terrestrial planet accretionary genetics. *Earth and Planetary Science Letters*, ***487***, 221-229.

Birck, J. L., Barman, M. R., & Capmas, F. (1997). Re□Os isotopic measurements at the femtomole level in natural samples. *Geostandards newsletter*, ***21***(1), 19-27.

Buchwald, V. F. (1975). Handbook of Iron Meteorites. University of California Press, 1418 pp. evols.library.manoa.hawaii.edu/handle/10524/35673.

Burkhardt, C., Kleine, T., Oberli, F., Pack, A., Bourdon, B., & Wieler, R. (2011). Molybdenum isotope anomalies in meteorites: constraints on solar nebula evolution and origin of the Earth. *Earth and Planetary Science Letters*, ***312***(3-4), 390-400.

Budde, G., Burkhardt, C., Brennecka, G. A., Fischer-Gödde, M., Kruijer, T. S., & Kleine, T. (2016). Molybdenum isotopic evidence for the origin of chondrules and a distinct genetic heritage of carbonaceous and non-carbonaceous meteorites. *Earth and Planetary Science Letters*, ***454***, 293-303.

Chabot, N. L. (2004). Sulfur contents of the parental metallic cores of magmatic iron meteorites. *Geochimica et Cosmochimica Acta*, *68*(17), 3607-3618.

Chabot, N. L., & Jones, J. H. (2003). The parameterization of solid metal□liquid metal partitioning of siderophile elements. Meteoritics & Planetary Science, **38**(10), 1425-1436.

Chabot, N. L., Wollack, E. A., McDonough, W. F., Ash, R. D., & Saslow, S. A. (2017). Experimental determination of partitioning in the Fe□Ni system for applications to modeling meteoritic metals. *Meteoritics & planetary science*, ***52***(6), 1133-1145.

Chabot, N. L., Understanding iron meteorites and early Solar System metallic cores of asteroid parent bodies (Vol. 12, EPSC2018-108). European Planetary Science Congress 2018.

Chen, J. H., Papanastassiou, D. A., & Wasserburg, G. J. (2010). Ruthenium endemic isotope effects in chondrites and differentiated meteorites. *Geochimica et Cosmochimica Acta*, ***74***(13), 3851-3862.

Cohen, A. S., & Waters, F. G. (1996). Separation of osmium from geological materials by solvent extraction for analysis by thermal ionisation mass spectrometry. *Analytica Chimica Acta*, ***332***(2-3), 269-275.

Dauphas, N., Davis, A. M., Marty, B., & Reisberg, L. (2004). The cosmic molybdenum–ruthenium isotope correlation. *Earth and Planetary Science Letters*, ***226***(3-4), 465-475.

Fegley B. and Palme H. (1985) Evidence for oxidizing conditions in the solar nebula from Mo and W depletions in refractory inclusions in carbonaceous chondrites. *Earth and Planetary Science Letters* **72**, 311–326.

Fischer-Gödde, M., Becker, H., & Wombacher, F. (2010). Rhodium, gold and other highly siderophile element abundances in chondritic meteorites. *Geochimica et Cosmochimica Acta*, ***74***(1), 356-379.

Fischer-Gödde, M., Burkhardt, C., Kruijer, T. S., & Kleine, T. (2015). Ru isotope heterogeneity in the solar protoplanetary disk. *Geochimica et Cosmochimica Acta*, ***168***, 151-171.

Goldstein, J. I., Scott, E. R. D., & Chabot, N. L. (2009). Iron meteorites: Crystallization, thermal history, parent bodies, and origin. *Chemie der Erde-Geochemistry*, ***69***(4), 293-325.

Hellmann, J. L., Kruijer, T. S., Van Orman, J. A., Metzler, K., & Kleine, T. (2019). Hf-W chronology of ordinary chondrites. *Geochimica et Cosmochimica Acta*.

Hilton, C. D., Bermingham, K. R., Walker, R. J., & McCoy, T. J. (2019). Genetics, crystallization sequence, and age of the South Byron Trio iron meteorites: New insights to carbonaceous chondrite (CC) type parent bodies. *Geochimica et Cosmochimica Acta*, ***251***, 217-228.

Horan M.F., Walker R.J., Morgan J.W., Grossman J.N., Rubin A.E. (2003) Highly siderophile elements in chondrites. *Chem. Geol.* ***196***, 5-20.

Jones, J. H., & Malvin, D. J. (1990). A nonmetal interaction model for the segregation of trace metals during solidification of Fe-Ni-S, Fe-Ni-P, and Fe-Ni-SP alloys. *Metallurgical transactions B*, ***21***(4), 697-706.

Kleine, T., Mezger, K., Münker, C., Palme, H., & Bischoff, A. (2004). 182Hf-182W isotope systematics of chondrites, eucrites, and martian meteorites: Chronology of core formation and early mantle differentiation in Vesta and Mars1. *Geochimica et Cosmochimica Acta*, ***68***(13), 2935-2946.

Kleine, T., & Walker, R. J. (2017). Tungsten isotopes in planets. *Annual review of earth and planetary sciences*, *45*, 389-417.

Kruijer, T. S., Kleine, T., Fischer-Gödde, M., Burkhardt, C., & Wieler, R. (2014a). Nucleosynthetic W isotope anomalies and the Hf–W chronometry of Ca–Al-rich inclusions. *Earth and Planetary Science Letters*, ***403***, 317-327.

Kruijer, T. S., Touboul, M., Fischer-Gödde, M., Bermingham, K. R., Walker, R. J., & Kleine, T. (2014b). Protracted core formation and rapid accretion of protoplanets. *Science*, ***344***(6188), 1150-1154.

Kruijer, T. S., Burkhardt, C., Budde, G., & Kleine, T. (2017). Age of Jupiter inferred from the distinct genetics and formation times of meteorites. *Proceedings of the National Academy of Sciences*, 201704461.

Lu Q. and Masuda, A. (1994). The isotopic composition and atomic weight of molybdenum. *International Journal of Mass Spectrometry and Ion Processes*, ***130***(1-2), 65-72.

Ludwig, K. R. (2003). Users manual for ISOPLOT/EX, version 3. A geochronological toolkit for Microsoft Excel. *Berkeley Geochronology Center Special Publication*, (4).

McCoy, T. J., Corrigan, C. M., Nagashima, K., Reynolds, V. S., Ash, R. D., McDonough, W. F., Yang, J., Goldstein, J. I., & Hilton, C. D. (2019). The Milton pallasite and South Byron Trio Irons: Evidence for oxidation and core crystallization. *Geochimica et Cosmochimica Acta*.

McCoy, T. J., Walker, R. J., Goldstein, J. I., Yang, J., McDonough, W. F., Rumble, D., Chabot, N. L., Ash, R. D., Corrigan, C. M., Michael, J. R., & Kotula, P. G. (2011). Group IVA irons: New constraints on the crystallization and cooling history of an asteroidal core with a complex history. *Geochimica et Cosmochimica Acta*, **75**(22), 6821-6843.

Nagai, Y., & Yokoyama, T. (2014). Chemical separation of Mo and W from terrestrial and extraterrestrial samples via anion exchange chromatography. *Analytical chemistry*, *86*(10), 4856-4863.

Nanne, J. A., Nimmo, F., Cuzzi, J. N., & Kleine, T. (2019). Origin of the non-carbonaceous–carbonaceous meteorite dichotomy. *Earth and Planetary Science Letters*, ***511***, 44-54.

Pernicka, E., & Wasson, J. T. (1987). Ru, Re, OS, Pt and Au in iron meteorites. *Geochimica et Cosmochimica Acta*, ***51***(6), 1717-1726.

Poole, G. M., Rehkämper, M., Coles, B. J., Goldberg, T., & Smith, C. L. (2017). Nucleosynthetic molybdenum isotope anomalies in iron meteorites–new evidence for thermal processing of solar nebula material. *Earth and Planetary Science Letters*, ***473***, 215-226.

Rehkämper, M., & Halliday, A. N. (1997). Development and application of new iondashexchange techniques for the separation of the platinum group and other siderophile elements from geological samples. *Talanta*, ***44***(4), 663-672.

Rubin, A. E. (2018). Carbonaceous and noncarbonaceous iron meteorites: Differences in chemical, physical, and collective properties. *Meteoritics & Planetary Science*, ***53***(11), 2357-2371.

Rusk, B. (2009). Laser Ablation ICP-MS in the Earth Sciences: Current Practices and Outstanding Issues. *Economic Geology*, **104**(4), 601-602.

Schaudy, R., Watson, J. T., & Buchwald, V. F. (1972). The chemical classification of iron meteorites. VI. A reinvestigation of irons with Ge concentration lower than 1 ppm. *Icarus*, ***17***(1), 174-192.

Scott, E. R., & Wasson, J. T. (1975). Classification and properties of iron meteorites. *Reviews of Geophysics*, ***13***(4), 527-546.

Scott, E. R., & Wasson, J. T. (1976). Chemical classification of iron meteorites—VIII. Groups IC. IIE, IIIF and 97 other irons. *Geochimica et Cosmochimica Acta*, ***40*****(**1), 103-115.

Scott, E. R., Wasson, J. T., & Buchwald, V. F. (1973). The chemical classification of iron meteorites—VII. A reinvestigation of irons with Ge concentrations between 25 and 80 ppm. *Geochimica et Cosmochimica Acta*, ***37*****(**8), 1957-1983.

Scott, E. R. (1977). Composition, mineralogy and origin of group IC iron meteorites. *Earth and Planetary Science Letters*, ***37***(2), 273-284.

Trinquier, A., Birck, J. L., & Allegre, C. J. (2007). Widespread 54Cr heterogeneity in the inner solar system. *The Astrophysical Journal*, ***655***(2), 1179.

Trinquier, A., Elliott, T., Ulfbeck, D., Coath, C., Krot, A. N., & Bizzarro, M. (2009). Origin of nucleosynthetic isotope heterogeneity in the solar protoplanetary disk. *Science*, ***324***(5925), 374-376.

Touboul, M., & Walker, R. J. (2012). High precision tungsten isotope measurement by thermal ionization mass spectrometry. *International Journal of Mass Spectrometry*, ***309***, 109-117.

Vockenhuber, C., Oberli, F., Bichler, M., Ahmad, I., Quitté, G., Meier, M., Halliday, A.N., Lee, D.C., Kutschera, W., Steier, P., & Gehrke, R. J. (2004). New Half-Life Measurement of H f 182: Improved Chronometer for the Early Solar System. *Physical Review Letters*, ***93***(17), 172501.

Völkening, J., Köppe, M., & Heumann, K. G. (1991). Tungsten isotope ratio determinations by negative thermal ionization mass spectrometry. *International Journal of Mass Spectrometry and Ion Processes*, ***107***(2), 361-368.

Wasson, J. T. (1969). The chemical classification of iron meteorites—III. Hexahedrites and other irons with germanium concentrations between 80 and 200 ppm. *Geochimica et Cosmochimica Acta*, ***33***(7), 859-876.

Wasson, J. T. (1999). Trapped melt in IIIAB irons; solid/liquid elemental partitioning during the fractionation of the IIIAB magma. *Geochimica et Cosmochimica Acta*, ***63***(18), 2875-2889.

Walker, R. J., Horan, M. F., Morgan, J. W., Becker, H., Grossman, J. N., & Rubin, A. E. (2002). Comparative 187Re-187Os systematics of chondrites: Implications regarding early solar system processes. *Geochimica et Cosmochimica Acta*, ***66***(23), 4187-4201.

Walker, R. J., McDonough, W. F., Honesto, J., Chabot, N. L., McCoy, T. J., Ash, R. D., & Bellucci, J. J. (2008). Modeling fractional crystallization of group IVB iron meteorites. *Geochimica et Cosmochimica Acta*, ***72***(8), 2198-2216.

Walker, R. J. (2012). Evidence for homogeneous distribution of osmium in the protosolar nebula. *Earth and Planetary Science Letters*, *351*, 36-44.meteorites. *Geochimica et Cosmochimica Acta*, ***72***(8), 2198-2216.

Warren, P. H. (2011). Stable-isotopic anomalies and the accretionary assemblage of the Earth and Mars: A subordinate role for carbonaceous chondrites. *Earth and Planetary Science Letters*, ***311***(1-2), 93-100.

Worsham, E. A., Walker, R. J., & Bermingham, K. R. (2016). High-precision molybdenum isotope analysis by negative thermal ionization mass spectrometry. *International Journal of Mass Spectrometry*, ***407***, 51-61.

Worsham, E. A., Bermingham, K. R., & Walker, R. J. (2017). Characterizing cosmochemical materials with genetic affinities to the Earth: genetic and chronological diversity within the IAB iron meteorite complex. *Earth and Planetary Science Letters*, ***467***, 157-166.

Worsham, E. A., Burkhardt, C., Budde, G., Fischer-Gödde, M., Kruijer, T. S., & Kleine, T. (2019). Distinct evolution of the carbonaceous and non-carbonaceous reservoirs: Insights from Ru, Mo, and W isotopes. *Earth and Planetary Science Letters*, ***521***, 103-112.